



HAL
open science

Numerical investigation of salt-frost damage of pervious concrete at the scale of a few aggregates

Iliass Tahiri, Patrick Dangla, Matthieu Vandamme, Quoc Huy Vu

► To cite this version:

Iliass Tahiri, Patrick Dangla, Matthieu Vandamme, Quoc Huy Vu. Numerical investigation of salt-frost damage of pervious concrete at the scale of a few aggregates. *Cement and Concrete Research*, 2022, 162, pp.106971. 10.1016/j.cemconres.2022.106971 . hal-04186670

HAL Id: hal-04186670

<https://hal.science/hal-04186670>

Submitted on 24 Aug 2023

HAL is a multi-disciplinary open access archive for the deposit and dissemination of scientific research documents, whether they are published or not. The documents may come from teaching and research institutions in France or abroad, or from public or private research centers.

L'archive ouverte pluridisciplinaire **HAL**, est destinée au dépôt et à la diffusion de documents scientifiques de niveau recherche, publiés ou non, émanant des établissements d'enseignement et de recherche français ou étrangers, des laboratoires publics ou privés.

Numerical investigation of salt-frost damage of pervious concrete at the scale of a few aggregates

Iliass Tahiri^a, Patrick Dangla^{a,*}, Matthieu Vandamme^a and Quoc Huy Vu^b

^aNavier, Ecole des Ponts, Univ Gustave Eiffel, CNRS, Marne-la-Vallée, France

^bHolcim Innovation Center, 95 rue du Montmurier, F-38070 Saint Quentin Fallavier, France

ARTICLE INFO

Keywords:

Frost attacks
Frost damage
Freeze-thaw cycles
Pervious concrete
Numerical modeling

ABSTRACT

In this study, we aim to gain insight into the damage mechanisms of pervious concrete subject to frost attacks in the presence of salt. We perform numerical simulations using a poroelastic model on system geometries representing pervious concrete at the scale of one or a few aggregates: 1) one aggregate coated with cement paste, 2) one aggregated coated with a cracked layer of cement paste, and 3) two aggregates coated and bonded with cement paste. The numerical simulations indicate that the damage is more likely to occur at the contact between aggregates. Furthermore, we observe significant shear stress at the vicinity of the paste/aggregate interface. We undertake a thorough parametric study to evaluate the impact of various boundary conditions, initial conditions, and materials parameters on the stresses generated during one or several freeze-thaw cycles. The insights can provide guidelines to design pervious concretes with enhanced freeze-thaw durability.

1. Introduction

Pervious concrete is a cement-based material with a high volume of inter-granular pores: its intergranular porosity varies between 11 % to 35 % [1] and its permeability varies between 0.1 and 2 cm/s [2]. Pervious concrete is made of single-sized aggregates coated and bonded by a small layer of cement paste. The thickness of the paste coating the aggregates depends on various parameters such as paste rheology, aggregate size, and volume of paste [3]. Xie et al. [3] report thickness of cement paste between 0.2 and 0.6 mm. Pervious concrete has substantial benefits, for instance, allowing water to drain easily from the surface to the soil to avoid floods. Still, it is subject to durability challenges such as low resistance to freeze-thaw cycles and clogging. In fact, in cold regions, freeze-thaw cycles damage rapidly pervious concrete structures. Studies have shown that in saturated conditions and the presence of deicing salts, pervious concrete undergoes only a few cycles of freeze-thaw before partial or total damage [4]. The durability of different pervious concrete pavements in service in a wet, hard-freeze region is investigated in [5] using microscopic observations. The authors suspect that freeze-thaw attacks cause the observed damage. This damage manifests as cracks in the aggregates, cement paste, and interfacial transition zone (ITZ). This limit to the use of pervious concrete in cold climate regions pushed various researchers to tackle the problem of freeze-thaw durability of pervious concrete [6–9].

Freeze-thaw observed in cementitious materials has been studied for several decades by both experimental and theoretical approaches. There are two prominent families of damage mechanisms for cementitious materials subjected to frost attacks: internal damage and salt scaling [10].

On the one hand, internal damage occurs in the concrete bulk, when ice forms first in capillary pores. Ice formation induces a volume increase of 9% compared to liquid water. Therefore, water pressurization occurs in the smaller (and still unfrozen) pores due to additional volume induced by ice formation in the largest pores. According to the hydraulic pressure theory, the pressure that drives the flux away from freezing regions (pressurized zones) is the cause of damage from internal frost. Mechanically, if the tensile strength of the paste is inferior to the hydraulic pressure, damage occurs. This theory explains the role of air voids in reducing the hydraulic pressure as unfrozen water can flow toward the air voids. However, it does not take into account the presence of salt. To tackle this, Powers [11] proposed the osmotic pressure theory. The theory postulates that when the ice starts to form in a porous medium saturated with a saline solution, the salt concentration of the remaining solution increases. The difference in salt concentration between

*Corresponding author

 patrick.dangla@univ-eiffel.fr (P. Dangla)

ORCID(s):

49 the zone of high concentration and other surrounding saturated zones with lower concentrations will result in water
50 diffusion from low to high concentration zones. Therefore, the fluid pressure will rise in the zone of high concentration
51 and induce tensile stress in the cement matrix. Valenza and Scherer [12] reported that this induced stress surpasses
52 concrete tensile strength only if the difference in salt concentration reaches approximately 14 %. Therefore, the authors
53 concluded that the osmotic pressure would never reach damaging levels for concrete since the fluid flow will rapidly
54 dissipate the rising pressure.

55 On the other hand, salt scaling consists of the debonding of small flakes at the surface of cementitious materials
56 upon freezing a saline solution on the surface. The maximum damage occurs with a concentration of solute of about
57 3 wt% [13, 14]. The existence of this pessimum has been proved experimentally by various studies. According to the
58 glue-spall theory [12], as the freezing occurs, ice and concrete contract at different rates (as the coefficient of thermal
59 expansion of ice is five times larger than that of concrete). The ice cracks around brine pockets to form ice islands.
60 When the salt concentration of the solution is low, the formed ice is strong enough not to crack, whereas, when its
61 salt concentration is high, the formed ice is too weak to propagate cracking into the concrete. Other mechanisms are
62 proposed to explain salt scaling, such as damage caused by the pressure of brine forced from the outer ice layer into
63 the concrete Yener [15].

64 Various studies use the poroelastic approach to model frost attack of cement-based materials [16–18]. According
65 to Coussy [19], the following mechanisms can explain the deformation of a material under freezing: 1) density change
66 when ice forms, which results in a rise of pore pressure, 2) pressure associated with interfacial energy between the
67 various constituents, 3) pressure associated to the transfer of water due to ice crystallization, 4) the cryosuction process,
68 and finally, 5) the thermomechanical coupling between the various constituents (solid matrix and the pressurized pores).
69 Various conditions such as full or partial saturation, air voids, and salt can impact the freezing behavior. Eriksson et al.
70 [20] developed a model of freezing behavior of partially saturated air-entrained concrete. However, this model does
71 not take into account the presence of salt in the solution. To overcome this limitation, they developed another model,
72 which considers the presence of salt in the solution, as well as the freeze-thaw hysteresis in a partially saturated air-
73 entrained concrete [21]. In the work of Rhardane et al. [22], the developed model considers the presence of salt, the
74 saturation degree, and the osmotic pressure to assess the freeze-thaw damage mechanisms of cementitious materials
75 at the cement paste microscale. Finally, at the scale of aggregates coated with cement paste, Rahman and Grasley [18]
76 developed a model to investigate the impact of freeze-thaw cycles in saturated conditions on one aggregate coated with
77 cement paste.

78 In this study, we investigate the behavior of pervious concrete under freeze-thaw solicitations, which is a topic
79 of societal interest, as those materials, which make it possible to alleviate soil impermeabilization, are sensitive to
80 freeze-thaw damage. Our goal is to simulate the impact of freeze-thaw cycles on an individual aggregate coated
81 with cement paste and two aggregates coated and bonded with cement paste. We work on these systems to provide
82 information on the mechanisms of freeze-thaw damage at the local scale of the cement coating, the aggregates, and
83 the paste/aggregate interface. Moreover, since the permeability of pervious concrete is high (because the macrovoids
84 pore structure is interconnected), it is likely that no hydraulic pressure develops in the macrovoids during freezing,
85 which is an additional reason to focus on the scale of a few aggregates. We utilize numerical simulations based on a
86 poromechanical model, which considers relevant processes for freezing porous solids. These processes are hydraulic
87 pressure, cryosuction, salt diffusion, and brine pockets at the material's surface. The combined equations describing
88 the complex phenomena in a porous material are solved using the finite element method in three dimensions at the scale
89 of two aggregates coated and bonded with cement paste. To the best of our knowledge, our work is the first application
90 of poromechanical freeze-thaw modeling to pervious concrete at the relevant scale of a few aggregates coated with
91 cement paste.

92 In the following section, we derive the poromechanical model necessary to simulate freeze-thaw in porous materi-
93 als. We present the details of the simulations and the adopted geometry in Sections 2.2 and 2.3, respectively. Section
94 2.4 details the initial conditions, boundary conditions, and the properties used for the simulations. Regarding, bound-
95 ary conditions, we propose a method for modeling brine pockets with different levels of connectivity. Section 3.1
96 presents the results obtained on an individual aggregate coated with cement paste and discusses the impact of various
97 parameters (i.e., the effect of salt, the effect of time and the number of freeze-thaw cycles, the effect of boundary con-
98 ditions, the effect of materials properties, and the influence of a crack in the cement paste). Section 3.2 presents the
99 results of simulations on the system of two aggregates coated and bonded with cement paste. We discuss the zones
100 where damage is most likely to occur in Section 3.3, before concluding. To do so, we concatenate the poromechanical
101 model for freeze-thaw with adequate failure criteria for bulk phases (i.e., cement paste and aggregates) and for the

102 paste/aggregate interface.

103 2. Model

104 This section describes the main equations of the model used to simulate freeze-thaw cycles of aggregates sur-
 105 rounded with cement paste and immersed in a salt solution. The section also provides the necessary inputs to conduct
 106 the simulations of frost attacks. Later in the manuscript, we discuss the effect of the number of freeze-thaw cycles (see
 107 Section 3.1.2), the impact of initial conditions (see Section 3.1.3), and the impact of boundary conditions (see Section
 108 3.1.4) on the system response to freeze-thaw.

109 2.1. Poroelastic model

110 We can use the poromechanical approach to describe the phenomena that occur in cement-based materials. This
 111 approach gives access to saturation and stresses during the process of freezing in concrete, for instance. Two phases
 112 coexist when freezing saturated porous solids: liquid water (which contains dissolved salt) and ice crystals. We define
 113 ϕ_J as the Lagrangian porosity. The fact that this porosity is Lagrangian means that, by definition, $\phi_J = V_J/V_0$, where
 114 V_J is the actual volume occupied by phase J and V_0 is the volume of the porous solid in the reference state. The partial
 115 Lagrangian porosity ϕ_J can be expressed as [23]:

$$\phi_J = \phi_0 S_J + \varphi_J \quad (1)$$

116 where ϕ_0 is the initial porosity, S_J is the Lagrangian saturation of the phase J. Eq. 1 states that this volume can vary
 117 because of two reasons: 1) because S_J varies, or because φ_J varies. Those two terms represent two different physical
 118 processes. The term $\phi_0 S_J$ takes into account variations of porosity occupied by phase J due to displacement of the
 119 meniscus separating phase J from the other phases. The term φ_J takes into account variations of porosity occupied by
 120 phase J due to deformation of the pore volume currently occupied by the phase J.

121 During the freezing of saturated cement-based material, the saturation of each phase is the fraction of pore volume
 122 occupied by the various phases. In this work, we consider that the material is saturated with water initially. At any
 123 time during the freezing process, the total Lagrangian porosity ϕ is the sum of the partial Lagrangian porosities ϕ_L
 124 and ϕ_C . In addition the liquid and ice the saturations verify the following equation:

$$S_L + S_C = 1 \quad (2)$$

125 In the followings we will neglect the deformation of pores, φ_J , in the conservation of mass for water and salt.

126 In any representative elementary volume, the total mass change is due to liquid solution transport between pores.
 127 The total mass is the mass of water and salt in liquid and solid states. We express the conservation of total mass by
 128 [24]:

$$\frac{\partial m_{total}}{\partial t} = -\nabla \cdot \mathbf{w}_L \quad (3)$$

129 where m_{total} is the total mass content and \mathbf{w}_L is the total mass flow vector.

130 The total mass content m_{total} is given by:

$$m_{total} = (\rho_L S_L + \rho_C S_C) \phi_0 \quad (4)$$

131 where ρ_L and ρ_C are the liquid water and ice density, respectively.

132 We express the conservation of salt mass by [24]:

$$\frac{\partial m_{salt}}{\partial t} = -\nabla \cdot \mathbf{w}_{salt} \quad (5)$$

133 where m_{salt} is the mass of salt and \mathbf{w}_{salt} is the mass flow vector of salt.

134 The mass of salt m_{salt} is given by:

$$m_{salt} = \rho_{salt} S_L \phi_0 \quad (6)$$

135 where ρ_{salt} is the mass salt concentration in the pore solution.

136 The liquid transport through the porous medium due to a pressure gradient can be modeled with Darcy's law [25]:

$$\mathbf{w}_L = -\rho_L k_{rl} \frac{k_{int}}{\mu_L} \nabla p_L \quad (7)$$

137 where $k_{rl} = k_{rl}(S_L)$ is the relative permeability, k_{int} is the intrinsic permeability, $\mu_L = \mu_L(T)$ is the viscosity of the
138 liquid phase, here considered to depend on temperature T only and p_L the liquid pore pressure.

The mass flow vector \mathbf{w}_{salt} of salt is:

$$\mathbf{w}_{salt} = M_{salt} \frac{c_s}{\rho_L} \mathbf{w}_L + \mathbf{j}_{salt} \quad (8)$$

139 where M_{salt} is the molar mass of salt, $\rho_{salt} = M_{salt} c_s$ is the mass salt concentration in the pore solution, c_s is the molar
140 salt concentration, and \mathbf{j}_{salt} is the diffusive salt flux.

141 The salt transport through the porous media can be modeled with Fick's law [25]:

$$\mathbf{j}_{salt} = -M_{salt} \phi S_L \tau D_{salt} \nabla(c_s) \quad (9)$$

142 where $\tau = \tau(\phi_0, S_L)$ is the tortuosity coefficient, D_{salt} is the molecular diffusion coefficient of salt in water.

143 The density ρ_J , of the phase J depends on the pressure p_J , temperature T , and salt concentration ρ_{salt} . They are
144 given by [17]:

$$\rho_C = \rho_C^0 \left[1 - \alpha_C(T - T_m) + \frac{p_C - p_m}{K_C} \right] \quad (10)$$

$$\rho_L = \rho_L^0 \left[1 - \alpha_L(T - T_m) + \frac{p_L - p_m}{K_L} - \rho_{salt} \tilde{V}_{salt} \right] \quad (11)$$

145 where ρ_J^0 is the density of phase J in the reference state (namely at atmospheric pressure $p_m = 101.325$ kPa and at
146 melting temperature $T_m = 0$ °C), α_J its coefficient of thermal expansion, K_J its bulk modulus, and \tilde{V}_{salt} is the relative
147 partial specific volume of salt (in $\text{m}^3 \cdot \text{kg}^{-1}$). We summarize the value of liquid and ice crystals parameters in Table 1.

148 The relative partial specific volume \tilde{V}_{salt} of salt is calculated using the following equation:

$$\tilde{V}_{salt} = \frac{V_{\text{NaCl}}}{M_{\text{NaCl}}} - \frac{V_{\text{H}_2\text{O}}}{M_{\text{H}_2\text{O}}} \quad (12)$$

149 where V_{NaCl} and $V_{\text{H}_2\text{O}}$ are the partial molar volumes of salt and liquid water, respectively, and where M_{NaCl} and $M_{\text{H}_2\text{O}}$
150 are their molar mass, respectively.

151 The conservation of heat in a porous material under freezing can be modeled by the following equation reported
152 in Zeng et al. [16]:

$$\frac{\partial s}{\partial t} = -\nabla \cdot s_L \mathbf{w}_L - \frac{1}{T} \nabla \cdot \mathbf{q} \quad (13)$$

153 where $s = s_{sol} + (\rho_L s_L S_L + \rho_C s_C S_C) \phi_0$ is the total entropy, and s_{sol} is the entropy of the solid skeleton.

Parameter	Value	Unit	Significance	Source
K_L	1.8	GPa	Bulk modulus of liquid water	[17]
K_C	7.8	GPa	Bulk modulus of ice crystals	[17]
C_L	4180	J.kg ⁻¹ .K ⁻¹	Heat capacity of liquid water	[26]
C_C	2000	J.kg ⁻¹ .K ⁻¹	Heat capacity of ice crystals	[26]
λ_L	0.6	W.m ⁻¹ .K ⁻¹	Thermal conductivity of liquid water	[26]
λ_C	2.2	W.m ⁻¹ .K ⁻¹	Thermal conductivity of ice crystals	[26]
$\alpha_L(T)$	$68.7 \cdot 10^{-6} + 13.877 \cdot 10^{-6} (T - T_m)$	K ⁻¹	Coefficient of thermal expansion of liquid water	[27]
α_C	$155 \cdot 10^{-6}$	K ⁻¹	Coefficient of thermal expansion of ice crystals	[17]
V_{NaCl}	$16.6 \cdot 10^{-6}$	m ³ .mol ⁻¹	Partial molar volume of salt	[28]
V_{H_2O}	$18.0 \cdot 10^{-6}$	m ³ .mol ⁻¹	Partial molar volume of liquid water	[29]
M_{H_2O}	$18.0 \cdot 10^{-3}$	kg ⁻¹ .mol ⁻¹	Molar mass of water	
M_{NaCl}	$58.4 \cdot 10^{-3}$	kg ⁻¹ .mol ⁻¹	Molar mass of salt	
ρ_L^0	1000.0	kg.m ⁻³	density of liquid in the reference state	
ρ_C^0	917.0	kg.m ⁻³	density of ice in the reference state	
s_m	23.54	J.mol ⁻¹ .K ⁻¹	Entropy of fusion of ice	

Table 1

Liquid water and ice crystals inputs for the simulations.

154 The specific entropy s_J of each phase depends on its pressure p_J , its heat capacity C_J , its thermal expansion
 155 coefficient α_J , and the temperature T [17] [30]:

$$s_L = s_L^0 + C_L \ln \frac{T}{T_m} - \frac{\alpha_L}{\rho_L^0} (p_L - p_m) \quad (14)$$

$$s_C = s_C^0 + C_C \ln \frac{T}{T_m} - \frac{\alpha_C}{\rho_C^0} (p_C - p_m) - s_m / M_{H_2O} \quad (15)$$

156 where the reference specific entropy s_J^0 is defined as the specific entropy of phase J at temperature T_m and pressure p_m .

157 The entropy s_{sol} of the solid skeleton is given by:

$$s_{sol} = C_s \ln \frac{T}{T_m} \quad (16)$$

158 where C_s is the specific heat capacity of the solid skeleton.

159 Fourier's law governs heat conduction. This law relates the rate of heat transfer to the gradient of temperature in
 160 the material [24]:

$$\mathbf{q} = -\lambda \nabla T \quad (17)$$

161 where \mathbf{q} is the heat flow vector, $\lambda = \lambda(\lambda_{sol}, \lambda_L, \lambda_C, S_L, \phi_0)$ is the thermal conductivity of the porous material, which
 162 takes into account the thermal conductivity of the various phases: λ_{sol} for the solid phase, λ_C for the ice crystals, and
 163 λ_L for the liquid water.

164 Hashin and Shtrikman [31] proposed a model to estimate the thermal conductivity of isotropic composite materials:

$$\lambda = \lambda_s + \frac{\phi_0}{\frac{1 - \phi_0}{3\lambda_s} + \frac{1}{S_L \lambda_L + (1 - S_L) \lambda_C - \lambda_s}} \quad (18)$$

165 The equation of mechanical equilibrium in absence of body forces is [24]:

$$\nabla \cdot \boldsymbol{\sigma} = 0 \quad (19)$$

166 The constitutive equations for a linear isotropic thermoporoelastic material with a porosity filled by liquid and ice
167 phases can be expressed as [24]:

$$\boldsymbol{\sigma} = \left(K - \frac{2}{3} G \right) \epsilon \mathbf{I} + 2G\boldsymbol{\epsilon} - [b_C p_C + b_L p_L + 3\alpha K (T - T_m)] \mathbf{I} \quad (20)$$

168 where \mathbf{I} is the second-order identity tensor, b_L and b_C denote the liquid and ice Biot coefficients, respectively, $\boldsymbol{\epsilon}$ is the
169 strain tensor, $\epsilon = tr(\boldsymbol{\epsilon})$ is the volume strain, $\boldsymbol{\sigma}$ is the stress tensor, α is the coefficient of thermal expansion of the dry
170 porous solid, K is the drained bulk modulus of the porous solid.

171 The linearized strain tensor $\boldsymbol{\epsilon}$ is defined by:

$$\boldsymbol{\epsilon} = \frac{1}{2} (\nabla \mathbf{u} + \nabla^T \mathbf{u}) \quad (21)$$

172 where \mathbf{u} is the displacement vector.

173 The local thermodynamic equilibrium of liquid water and ice (i.e., the equality of their chemical potentials) yields
174 the Thomson equation:

$$p_C = p_m + \frac{1}{V_C} \left[V_{\text{H}_2\text{O}}(p_L - p_m) - s_m(T - T_m) + R_g T \ln(a_w(c_s, T)) \right] \quad (22)$$

175 where p_C is the ice pressure, V_C is the ice molar volume, R_g is the ideal gas constant, s_m is the entropy of fusion
176 of ice, c_s is the salt concentration, and $a_w(c_s, T)$ is the water activity. The water activity is calculated as function of
177 temperature and salt concentration using the model developed by Lin and Lee [32, 33].

178 To link the macroscopic poroelastic properties to the elastic properties of the skeleton and saturation, we use the
179 following equations [23]:

$$b = b_L + b_C \quad (23)$$

$$b_J = bS_J \quad (24)$$

180 During freezing, there exists a threshold size such that all pores with an entry radius smaller than this threshold
181 are filled with liquid phase and all pores with an entry radius larger than this threshold are filled with ice. During
182 thawing, this threshold size is such that all pores with a size smaller than this threshold are filled with liquid phase and
183 all pores with a size larger than this threshold are filled with ice. For poromechanical calculations, rather than in how
184 this threshold size varies during the solicitation (see Figure 1 for a few cases), we are interested in how the saturation
185 S_L varies during the solicitation. How this liquid saturation evolves is related to the capillary pressure through the Van
186 Genuchten relation. The Van Genuchten model provides a retention curve that relates the liquid saturation S_L with the
187 capillary pressure ($p_C - p_L$) [34]:

$$S_L = \left[1 + \left(\frac{p_C - p_L}{n} \right)^{\frac{1}{1-m}} \right]^{-m} \quad (25)$$

188 where n and m are constants related to the pore structure of the porous solid.

189 Upon freezing, blockage of the pore by ice reduces the permeability of the material. We relate the permeability to
190 the retention curve with the Mualem model [35]:

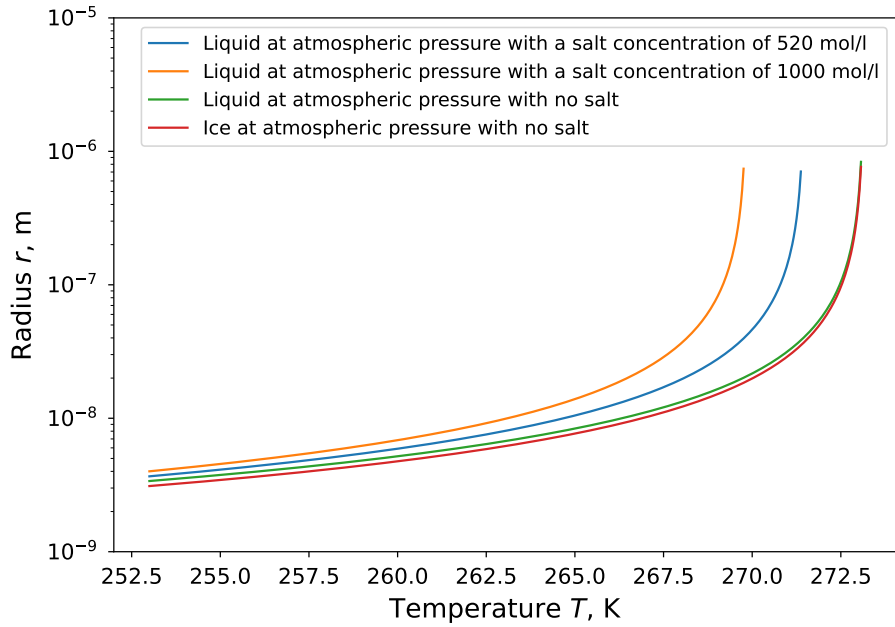


Figure 1: Threshold size of interest during freeze-thaw problems. All pores with an entry radius (respectively a radius) smaller than this threshold remain full of liquid phase during freezing (respectively thawing). All other pores are filled with ice.

$$k_{rl} = \sqrt{S_L} \left(1 - \left(1 - S_L^{1/m} \right)^m \right)^2 \quad (26)$$

191 The combination of the previous equations is solved using the 3D finite element method (FEM) in the numerical
 192 solver BIL [36]. We generate the geometry and mesh with the meshing software GMSH [37]. We summarize the
 193 primary and the secondary variables in Table 2. The equations solved are Eqs. 3 to 11, 13 to 17, 19 to 22, and 25. One
 194 can check that there are as many scalar unknowns (i.e., 39) as scalar equations.

195 2.2. Simulations rationale

196 The goal of the model is to numerically simulate the effect of freeze-thaw cycles on pervious concrete at the scale
 197 of one or a few aggregates covered by cement paste. Studying a unique aggregate coated with cement paste allows us
 198 to quantify the interactions between aggregate and cement paste in pervious concrete. In particular, we also aim to
 199 study the impact of a crack in the cement layer. Studying a system of two aggregates coated and bonded with cement
 200 paste allows us to quantify what happens at the junction between two aggregates.

201 The simulations are performed for various boundary and initial conditions to gain insights on the extent of the
 202 influence of these entry conditions, which are difficult to quantify experimentally. We also investigate the influence of
 203 cement paste and aggregate properties on the response to freeze-thaw cycles.

204 2.3. Geometry

205 For our numerical simulations, we consider three model systems: 1) a spherical aggregate of diameter 8 mm coated
 206 with a cement paste of thickness 300 μm , 2) a spherical aggregate of diameter 8 mm coated with a cement paste of
 207 thickness 300 μm in the presence of a crack, 3) two spherical aggregates of diameter 8 mm coated and bonded with a
 208 cement paste of thickness 300 μm .

209 Figure 2 presents the geometries and the mesh considered for this study. Due to the symmetry of the problems,
 210 we model the individual aggregate coated with intact cement paste as a one-dimensional system. For the aggregate
 211 coated with a cracked layer of cement paste, we model only half a sphere and perform two-dimensional axisymmetric

State variable	Significance	Number of scalar unknowns	Type of variable
T	Temperature	1	Primary
c_s	Salt concentration	1	Primary
p_L	Liquid pressure	1	Primary
\mathbf{u}	Displacement vector	3	Primary
m	Total mass of solution per unit volume	1	Secondary
\mathbf{w}_L	Mass flow vector of solution	3	Secondary
\mathbf{m}_{salt}	Mass of salt per unit volume	1	Secondary
\mathbf{w}_{salt}	Mass flow vector of salt	3	Secondary
\mathbf{j}_{salt}	Diffusive salt flux vector	3	Secondary
s_L	Entropy of liquid	1	Secondary
s_C	Entropy of ice	1	Secondary
s_{sol}	Entropy of solid	1	Secondary
\mathbf{q}	Heat flow vector	3	Secondary
$\boldsymbol{\sigma}$	Stress tensor	6	Secondary
p_C	Pressure in ice	1	Secondary
S_L	Lagrangian saturation in liquid water	1	Secondary
ρ_L	Density of solution	1	Secondary
ρ_C	Density of ice crystal	1	Secondary
$\boldsymbol{\epsilon}$	Strain tensor	6	Secondary

Table 2

Primary and secondary variables of the model.

212 simulations (see Figure 2-a). For the two bonded aggregates, we model a quarter of the geometry, again performing
 213 two-dimensional axisymmetric simulations (see Figure 2-b).

214 We use a Cartesian system of coordinates. Axes Ox and Oy are in the simulated plane, with Oy aligned with the
 215 axis of symmetry. The origin of the coordinate system is at the center of the aggregate. We will refer to the x -direction
 216 and the y -direction as horizontal and vertical directions, respectively.

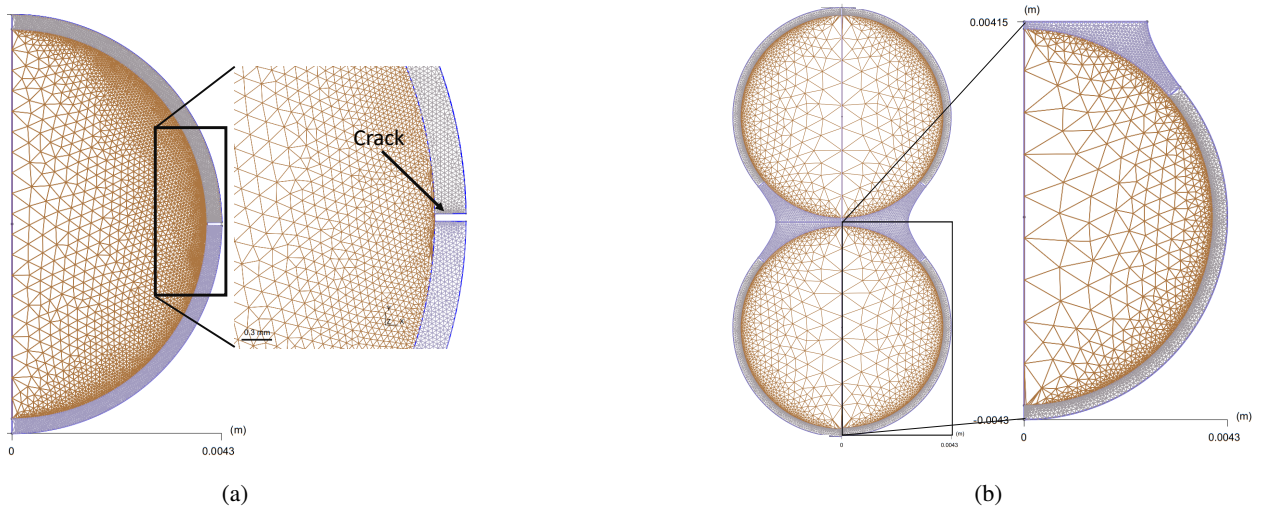


Figure 2: Modeled systems: (a) spherical aggregate coated with a cracked layer of cement paste, (b) two spherical aggregates coated and bonded with cement paste. The plane $y = 0.0041$ m is a plane of symmetry for this latter system.

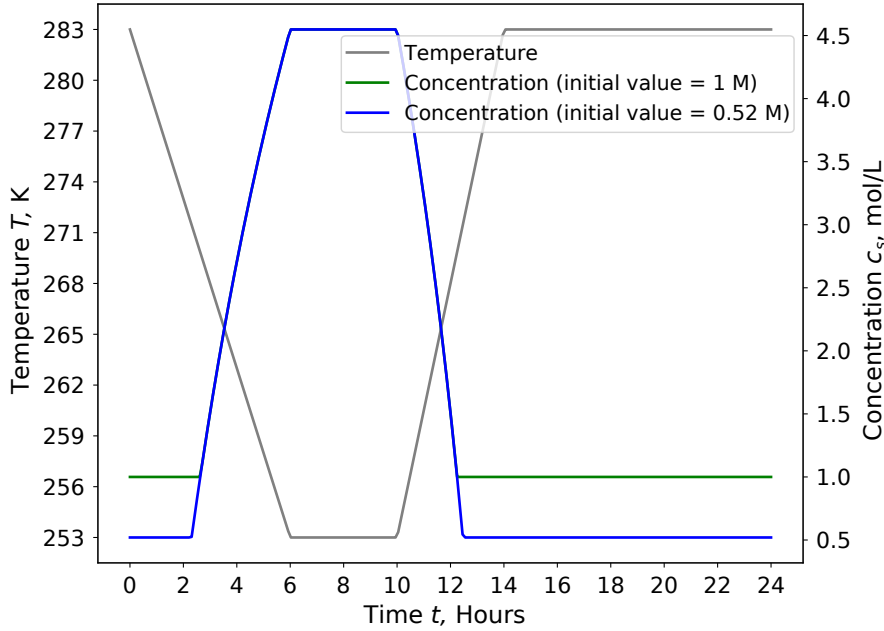


Figure 3: Temperature cycle and resulting salt concentration imposed at the boundary in the case of interconnected brine pockets.

2.4. Initial and boundary conditions

2.4.1. Initial conditions

We consider that both the aggregate and the cement paste are initially saturated with pure liquid water at a pressure p_L equal to the atmospheric pressure p_{atm} , i.e.:

$$p_L(t = 0) = p_{atm} \quad (27)$$

In Section 3.1.3, we will discuss the impact of this initial condition by considering that the samples are initially filled with a salt solution as if the salt present in the solution around the samples had time to diffuse throughout the medium before the start of the freeze-thaw cycles. In terms of temperature, for all systems, we consider that the initial temperature is homogeneous and equal to 10 °C.

2.4.2. Mechanical boundary conditions

For all systems, on the axis of symmetry $x = 0$, we prevent any horizontal displacement. The outer surface of the cement paste is free of stress. For the systems with one aggregate, we prevent vertical displacement of the bottom extremity of the system. For the system with two aggregates bonded by the cement paste, the top horizontal surface is a plane of symmetry. On this plane of symmetry, we impose no vertical displacement and no friction in the horizontal direction. Furthermore, the bottom extremity of the sphere is free.

2.4.3. Thermal boundary conditions

Starting from +10 °C, each freeze-thaw cycle, lasting 24 hours, consists in: 1) decreasing the temperature at a rate of -5 °C/h for 6 hours, down to a minimum temperature of -20 °C; 2) maintaining the sample at -20 °C for 4 hours; 3) increasing the temperature at a rate of +7.5 °C/h for 4 hours, back up to +10 °C; 4) maintaining the sample at +10 °C for 10 hours. We impose the temperature cycle on the outer boundary of the systems. The thermal cycle considered is displayed in Figure 3.

2.4.4. Hydraulic boundary conditions

We consider a null flux condition in the horizontal direction on the axis of symmetry of all systems.

When the temperature at boundaries is positive, the outer surface of the specimens is in contact with the salt solution at pressure $p_L = p_{atm}$ and concentration $c_s = 520$ mol/L corresponding to $\approx 3\%$ of the weight of water.

Parameter	Symbol	Unit	Value for cement paste	Source	Value for aggregate	Source
Porosity	ϕ_0	-	0.3	[50]	0.04	[24]
Intrinsic permeability	k_{int}	m ²	$1 \cdot 10^{-21}$	[42]	$1 \cdot 10^{-20}$	[47]
Young modulus	E	GPa	25	[38]	60	[44]
Poisson coefficient	ν	-	0.22	[50]	0.3	[45]
Biot coefficient	b	-	0.55	[50]	0.6	[24]
Thermal expansion of solid matrix	α_s	10^{-6} K^{-1}	17	[39]	2.2	[49]
Thermal conductivity of solid matrix	λ_s	$\text{W} \cdot \text{m}^{-1} \cdot \text{K}^{-1}$	0.53	[43]	2.8	[48]
Volumetric heat capacity of solid	C_s	$\text{J} \cdot \text{m}^{-3} \cdot \text{K}^{-1}$	$1.47 \cdot 10^6$	[51]	$1.9 \cdot 10^6$	[45]
Van Genuchten parameter	m	-	0.42	[16]	0.42	[16]
Van Genuchten parameter	n	MPa	16.28	[52]	16.28	[52]
Friction angle	θ	°	35	[53]	35	[44]

Table 3

Materials inputs for the simulations.

239 When freezing occurs, a mixture of ice and brine pockets surrounds the sample. At all instants, we consider that
 240 liquid water and ice outside the cement paste are in thermodynamic equilibrium (i.e., their chemical potentials are
 241 equal). Therefore, the Thomson equation (22) remains valid to relate the pressure of the solution in the pockets with
 242 the ice pressure. We consider interconnected brine pockets: the liquid pressure in these brine pockets and the ice
 243 pressure remain equal to the atmospheric pressure. Consequently, the Thomson equation (22) reduces to:

$$(T - T_m)S_m - R_g T \ln(a_w(c_s, T)) = 0 \quad (28)$$

244 which imposes a relationship between the temperature T and the concentration $c_s(T)$ on the system's boundaries. This
 245 relationship is displayed in Figure 3.

246 We observe in Figure 3 that the hypothesis that both ice and the brine pockets remain at atmospheric pressure
 247 implies that, upon freezing, the lower the temperature, the higher the concentration of salt in the brine pockets (i.e., on
 248 the boundaries of the system). This hypothesis also entails that no ice forms in the pores in the vicinity of the samples'
 249 surface because of the rise in salt concentration which lowers the melting temperature of the brine pocket.

250 In Section 3.1.4, we will assess the impact of this boundary condition by considering that the brine pockets are
 251 disconnected and that their pressure may differ from the atmospheric pressure.

252 2.5. Properties of aggregates, cement paste, and their interface

253 In the simulations, we focus on modeling a standard cement paste and a standard limestone aggregate. For cement
 254 paste, Young's modulus varies from 30 MPa for a water-to-cement ratio w/c of 0.35 to 15 GPa for a water-to-cement
 255 ratio of 0.6 [38]. The Poisson ratio is assumed equal to 0.2. The coefficient of thermal dilatation α_s of the solid skeleton
 256 varies from $13 \cdot 10^{-6} \text{ K}^{-1}$ to $20 \cdot 10^{-6} \text{ K}^{-1}$ [39–41]. The permeability of cement highly depends on its water-to-cement
 257 ratio and age. Cui and Cahyadi [42] report a permeability of $2.66 \cdot 10^{-22} \text{ m}^2$ for a cement paste with a water-to-cement
 258 ratio of 0.3 at 7 days of age and a permeability smaller than $2.69 \cdot 10^{-23} \text{ m}^2$ at 210 days of age. For a cement paste
 259 with a cement-to-water ratio of 0.4, the permeability at 7 days of age is $8.11 \cdot 10^{-21} \text{ m}^2$ and $1.22 \cdot 10^{-22} \text{ m}^2$ at 210 days
 260 of age. Heat conductivity of cement paste is $0.53 \text{ W} \cdot \text{m}^{-1} \cdot \text{K}^{-1}$ for cement without silica fume and $0.33 \text{ W} \cdot \text{m}^{-1} \cdot \text{K}^{-1}$
 261 for cement paste with silica fume as reported in Xu and Chung [43].

262 For limestone rocks, the static Young modulus ranges between 18 GPa and 66 GPa [44]. Poisson ratio for limestones
 263 vary from 0.11 to 0.45 [45]. Iscan et al. [46] report values of limestone water permeability that range from $1.67 \cdot 10^{-14}$
 264 m^2 to $2.27 \cdot 10^{-14} \text{ m}^2$. Porosities reported in this study range from 12 % to 18 %. Selvadurai and Głowacki [47] report
 265 for Cobourg limestones values of porosity of $1.5 \% \pm 0.2 \%$. This same study reports values of permeability in the
 266 range of $7 \cdot 10^{-18} \text{ m}^2$ to $2.7 \cdot 10^{-20} \text{ m}^2$. Thermal conductivity is reported to be $2.29\text{--}2.78 \text{ kcal} \cdot \text{m}^{-1} \cdot \text{h}^{-1} \cdot \text{°C}^{-1}$ [48]. The
 267 coefficient of thermal expansion α_s for pure limestone, basalt, granite and gneiss is reported to vary between 0.7 and
 268 $2.5 \cdot 10^{-6} \text{ °C}^{-1}$ [49]. For the volumetric heat capacity, Aurangzeb et al. [45] report values ranging from $1.6 \cdot 10^6$ to
 269 $2.2 \cdot 10^6 \text{ J} \cdot \text{m}^{-3} \cdot \text{K}^{-1}$. For limestone, Biot coefficient is reported to vary from 0.34 to 0.88 and porosity from 4 to 29 %
 270 [24].

271 Failure models are necessary to investigate the failure of the cement paste, the aggregate and the interface. Gu
 272 et al. [54] found that paste/aggregate interface failure can be modeled by a Mohr-Coulomb failure criterion, which can
 273 be described by the following equation:

$$|\tau| = c + (\sigma_{rr} + S_{LP_L} + S_{CP_C}) \tan(\theta) \quad (29)$$

274 where $\tau = \sigma_{r\theta}$ is shear stress acting on the interface, $\sigma_{rr} + S_{LP_L} + S_{CP_C}$ is the effective stress acting normal to the
 275 interface (We assume that all irreversible deformations occur at constant volume of the solid matrix, from which the
 276 effective stress that intervenes in the failure criterion is the Terzaghi effective stress (extended to partially saturated
 277 porous solid) [25].) and where c and θ are the cohesion and friction angle of the interface, respectively.

278 For the cement paste and aggregate, we consider a Drucker-Prager failure criterion, which can be expressed by the
 279 following equation:

$$f(\sigma_{eff}, \sigma_{VM}) = B\sigma_{eff} + \sigma_{VM} + A \quad (30)$$

280 where $\sigma_{eff} = \sigma_m + S_{LP_L} + S_{CP_C}$ is the effective mean stress, $\sigma_m = \frac{1}{3}tr(\sigma)$ is the mean stress, and σ_{VM} is the
 281 Von Mises stress (i.e., the second invariant of the deviatoric stress). The parameters A and B are called Drucker-
 282 Prager parameters. These parameters can be related to the friction angle θ and the cohesion c of the material [55].
 283 Drucker-Prager parameters can be calculated by the following equations:

$$A = \frac{6c \cos(\theta)}{\sqrt{3}(3 \pm \sin(\theta))} \quad (31)$$

$$B = \frac{2 \sin(\theta)}{\sqrt{3}(3 \pm \sin(\theta))} \quad (32)$$

284 For limestone rocks, the friction angle is reported to vary between 34.5 ° and 45 °. The cohesion is reported to be
 285 23.5 MPa [44]. For the cement paste, the friction angle is reported to vary between 25 ° to 65 ° [53]. For the interface,
 286 Gu et al. [54] showed that the friction angle does not depend on the aggregate roughness. The friction angle found in
 287 this study is 35 °, which is similar to values reported in Taylor and Broms [56]. The cohesion of the interface varies
 288 from 0.81 MPa to 7.31 MPa, according to this study. These values depend on the nature of the aggregate and its surface
 289 roughness. In this study, we consider that the friction angle for both the aggregate and the cement paste is equal to 35
 290 °.

291 We use the properties summarized in Table 3 for the aggregate and the cement paste for our simulations.

292 3. Results and discussion

293 3.1. Individual coated aggregate

294 This section first presents the effect of 1 freeze-thaw cycle on an aggregate coated with cement paste. Later in the
 295 manuscript, in Section 3.1.2, we discuss the impact of the number of freeze-thaw cycles. We also study the effect of
 296 various inputs and situations related to the initial and boundary conditions.

297 Simulations show that temperature varies almost homogeneously in the system: indeed, at all times, the temperature
 298 everywhere differs at maximum by 0.01 °C from the temperature imposed on the edges.

299 3.1.1. Qualitative description of the response to 1 freeze-thaw cycle

300 Figure 4 and Figure 5 provide the spatial distribution and temporal evolution of liquid saturation, liquid pore
 301 pressure, salt concentration, and ice pore pressure in the cement paste and the aggregate during one freeze-thaw cycle.
 302 Ice starts to form inside the larger pores upon freezing (i.e., when $T < T_m$). First, positive fluid pressure builds up
 303 due to the rapid volume increase imposed by ice formation (because of the difference in density between crystals and
 304 liquid water). At this stage, liquid water does not have enough time to escape the pores. While the freezing phase
 305 continues from 2 h to 6 h, a depression and over-pressure of the liquid is observed in Figure 5a. Ice continues to form
 306 in pores, and the liquid continues to flow to dissipate the pressure. However, with continuous ice formation, the relative
 307 permeability becomes lower and lower, which increases the time needed for the pore liquid pressure to dissipate. When

308 the ice blocks the pore, liquid finds it more difficult to travel through the material, and therefore the pressure rises until
 309 becoming positive. This competition between ice formation, permeability, and liquid pressure dissipation explains the
 310 decrease and increase of liquid pressure for the time intervals [2 h, 3 h] and [3 h, 5 h], respectively. Over the phase
 311 where the temperature is constant (during which $T = 253.15 \text{ K} = -20 \text{ }^\circ\text{C}$), no additional ice is formed in the material,
 312 as can be observed in Figure 5b. The liquid water pressure slowly dissipates when water moves from frozen pores to
 313 the outside. At the end of this phase, 10 h into the freeze-thaw cycle, the pore pressure did not have the time to dissipate
 314 completely by reaching the atmospheric pressure. At the beginning of the thawing phase, the ice starts melting and,
 315 since the molar volume of liquid water is smaller than that of ice, the liquid pore pressure decreases. Concurrently, the
 316 permeability increases.

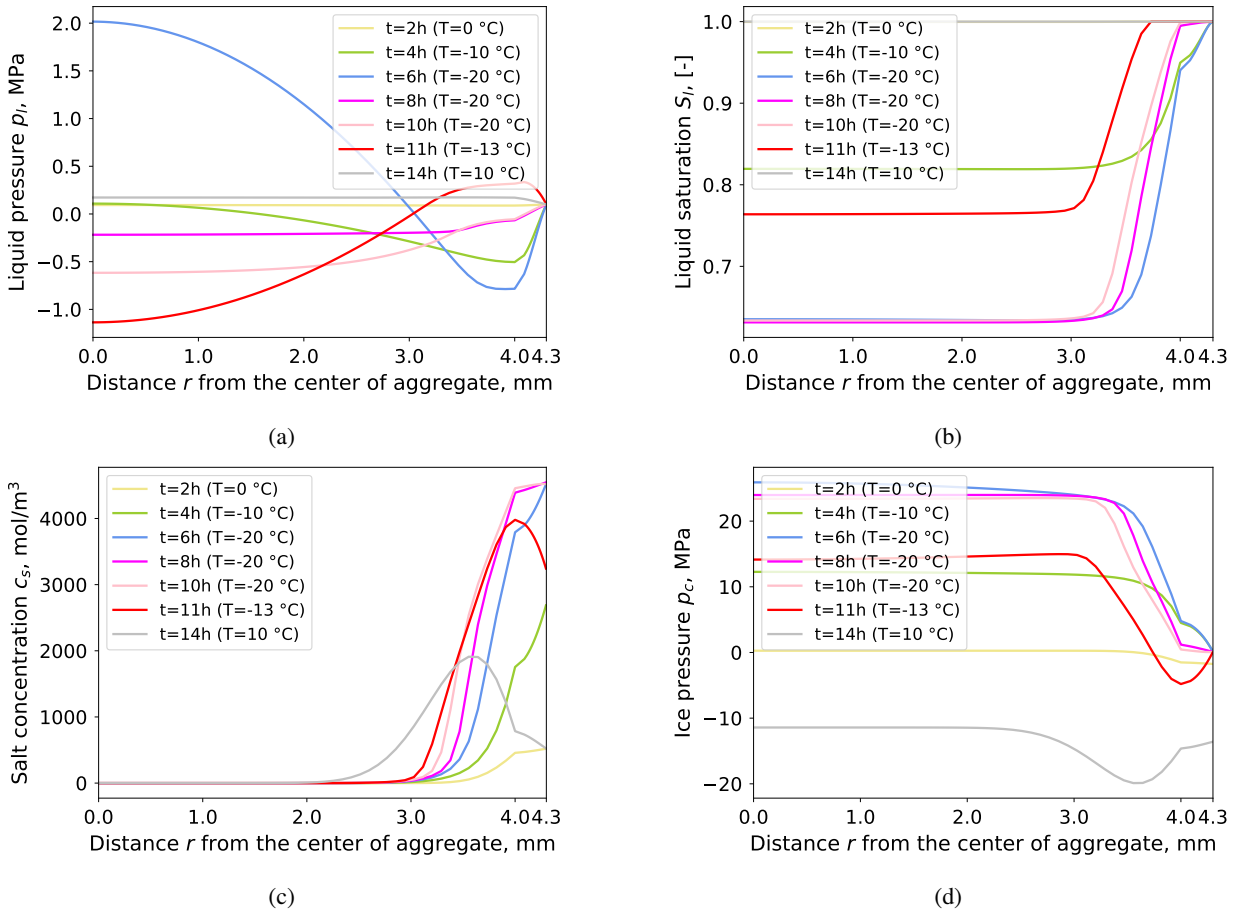


Figure 4: Spatial distribution of (a) liquid pressure, (b) liquid saturation, (c) salt concentration, and (d) ice pressure at various temperatures for an individual aggregate coated with cement paste.

317 At the boundary, the brine pockets with an increasing salt concentration lower the freezing point. Thus, there is no
 318 formation of ice in the pores at the vicinity of the outer surface. Figure 5 presents the variation of liquid pressure, liquid
 319 saturation, salt concentration, and ice pressure at the center of the aggregate (i.e., $r = 0.05 \text{ mm}$), at a position $r = 2 \text{ mm}$
 320 from the center of the aggregate, at the interface in both the cement paste and the aggregate, and at the outer boundary
 321 (i.e., $r = 4.3 \text{ mm}$). Note that when the ice saturation is equal to zero (liquid saturation equal to 1) the ice pressure,
 322 resulting from the Eq. 22, is fictitious and therefore not physical. This case is that of the negative values in Figs. 4d
 323 and 5d. We observe the minimal ice saturation in the cement paste, while the ice saturation is larger at the center of
 324 the aggregates than closer to the outer surface. With time, the salt diffusion process in the cement paste increases the
 325 liquid saturation in the zones reached by salt. The salt concentration at the boundary decreases when the temperature
 326 increases back (i.e., upon thawing). Salt near the surface starts migrating outside and inside the sample, where less
 327 salt is present. At the end of the first cycle, not all the salt that penetrated the sample during freezing diffused outside.

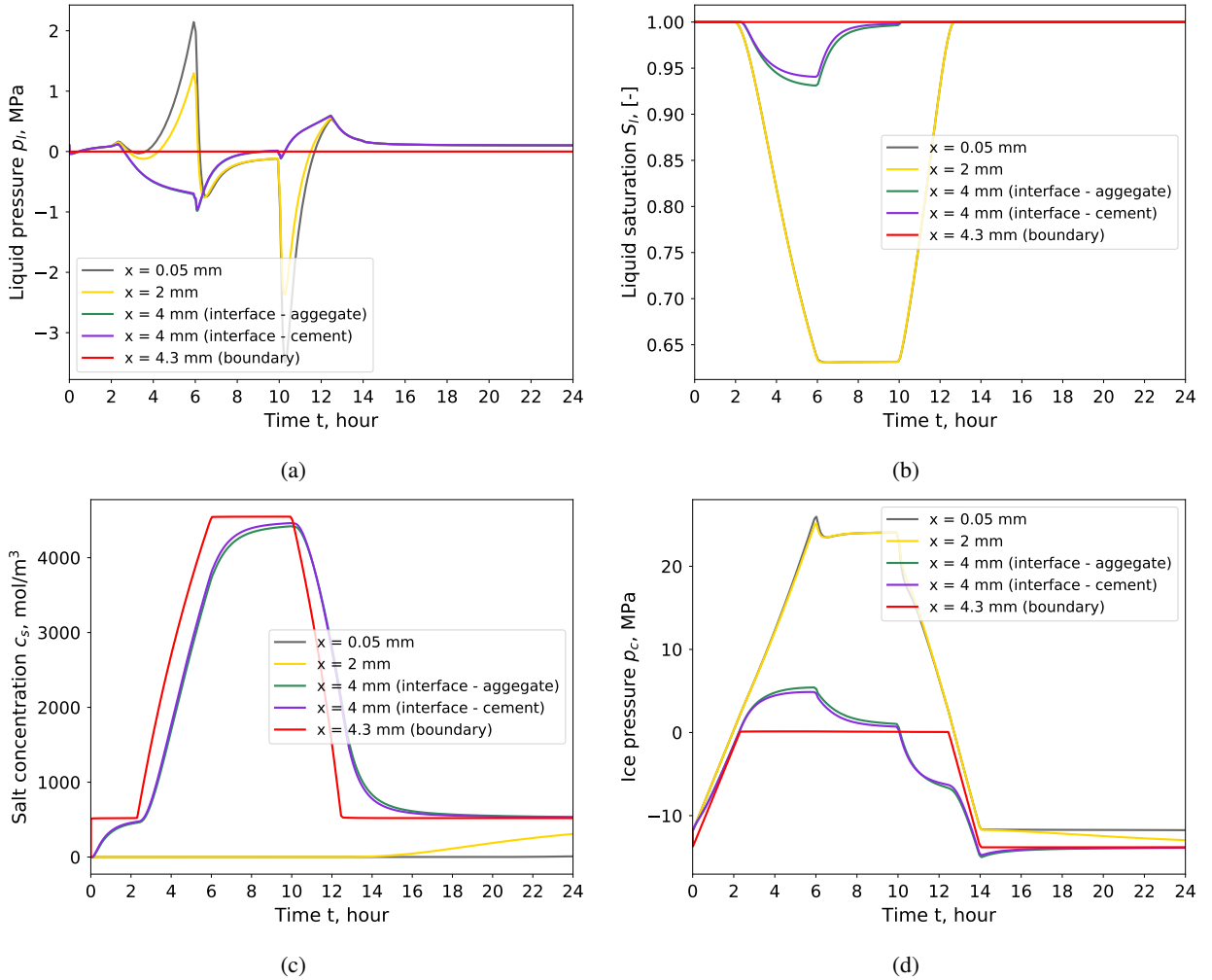


Figure 5: Evolution over time for various points of (a) liquid pressure, (b) liquid saturation, (c) salt concentration and (d) ice pressure in the individual aggregate coated with cement paste.

328 We will shed more light on these observations in Section 3.1.2.

329 Mechanically, liquid pressure variations, thermal behavior of the various phases, and boundary conditions control
 330 the stresses (and, consequently, the deformations). Figure 6 shows the resulting distribution of Von Mises (Figure
 331 6a) and effective mean stress (Figure 6b) at various temperatures during the freeze-thaw cycle. High shear stress is
 332 observed in the cement paste, reaching a maximum at the paste/aggregate interface. The effective mean stress curve
 333 shows that high stresses prevail in the cement paste and the aggregate. Concerning effective mean stress, the highest
 334 stresses are observed in the aggregate when reaching the minimal temperature of -20 °C.

335 3.1.2. Effect of time and of number of freeze-thaw cycles

336 Through the freeze-thaw cycles, we observe (Figure 7) that there is an accumulation of salt in pores. Upon freez-
 337 ing, salt penetrates the system, but not all salt flows back outside upon thawing. Therefore, the melting temperature
 338 decreases in the zone with larger salt content, implying lesser ice. This mechanism repeats itself, freeze-thaw cycle
 339 after freeze-thaw cycle, resulting in less ice formation in zones with high salt concentrations. Therefore, more salt in
 340 the pores after a larger number of freeze-thaw cycles helps lower the ice saturation in the pores. Furthermore, Figure
 341 7 shows that the maximal Von Mises stress decreases with an increasing number of freeze-thaw cycles. This decrease
 342 is because less ice crystallizes in regions with higher salt concentrations.

343 In actual materials, once the damage initiates, we know that some material properties differ from the initial ones.

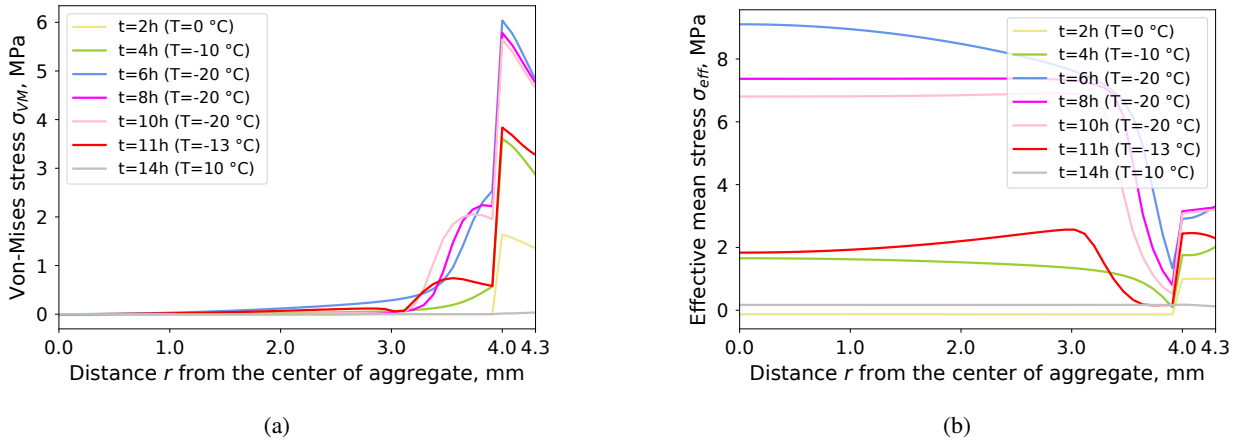


Figure 6: Spatial distribution of (a) Von Mises stress and (b) effective mean stress at various time steps for individual aggregate coated with cement paste.

344 For example, initiation of cracks in the cement matrix will result in a more permeable material with less mechanical
 345 resistance [57]. Thus, lower stresses can still result in a progression of damage over the cycles after damage initiation.
 346 With our present poroelastic model, we do not capture such damage. Damage laws should be incorporated into the
 347 modeling approach to better model the effect of repeated cycles on the evolution of stress distributions.

348 3.1.3. Role of salt

349 This section investigates the impact of initial saturation with a solution of NaCl at a concentration of 0, 100, 200,
 350 520 mol.m⁻³. We assume that salt has diffused through the whole cement paste before the freeze-thaw cycles. This
 351 hypothesis is reasonable because the cement paste thickness in pervious concrete is small (i.e., from 100 μm to 2
 352 mm). We consider that the freezing of the sample occurs in an outside salt solution with an initial concentration of
 353 520 mol.m⁻³. When the temperature becomes smaller than the solution's freezing point, some of the liquid water in
 354 the porosity turns into ice. When a given amount of pure liquid water freezes, its volume increases by +9%. In the
 355 presence of salt in the solution, increasing the concentration decreases the solution's freezing point. Upon freezing
 356 the salt solution, dissolved salt diffuses toward the still unfrozen part of the solution and the ice crystals formed are
 357 crystals of pure water. As shown in Figure 8, at -20 °C, the ice saturation decreases with an increasing initial salt
 358 concentration. Experimental data corroborate such observation: at a given temperature, in various porous media, the
 359 amount of unfrozen water determined by the NMR technique increases with an increasing solute concentration (may
 360 it be NaCl, KCl, MgCl₂) [58]. Upon an increase of salt concentration, less ice crystallizes in the pores, and therefore
 361 the pore pressures applied to the solid skeleton decrease. Said otherwise, the maximal magnitude of stresses in the
 362 cement paste and the aggregate decreases with an increasing salt concentration. Thus, the present poroelastic model
 363 predicts that the presence of salt in the pore fluid has a protecting effect against internal damage.

364 Figure 8 presents the Von Mises stress for three initial salt concentrations. The Von Mises stress in this configuration
 365 decreases with increasing initial salt concentration. One beneficial aspect of using deicing salt is that it lowers the ice
 366 melting temperature. Yuan Jie et al. [59] report that the volume variation during freezing of sodium chloride solution
 367 decreases with increasing salt concentrations. However, salt also presents negative effects, such as increasing the degree
 368 of saturation due to the concentration differences, potential osmotic pressures due to salt concentration gradient, and
 369 salt crystallization in the material's pores.

370 Experimentally, the presence of salt solution causes maximal damage for an intermediate salt concentration. This
 371 pessimum is at a salt concentration of ≈ 3% by weight for various types of salts [13, 14, 60, 61]. According to Yuan
 372 Jie et al. [59], the pessimum concentration is due to the competition between positive and negative aspects of NaCl
 373 on the freezing behavior, while Valenza and Scherer [12], with the glue-spall theory, rather attribute this pessimum to
 374 the impact of salt on the mechanical properties of the ice formed at the surface of the porous solid. In any case, the
 375 proposed model does not capture this pessimum, which shows that properly modeling this pessimum requires more
 376 physical ingredients (e.g., glue-spall) than those present in the model.

377 We think that the glue spall will occur in the inter-granular porosity. The ice that forms within these macrovoids

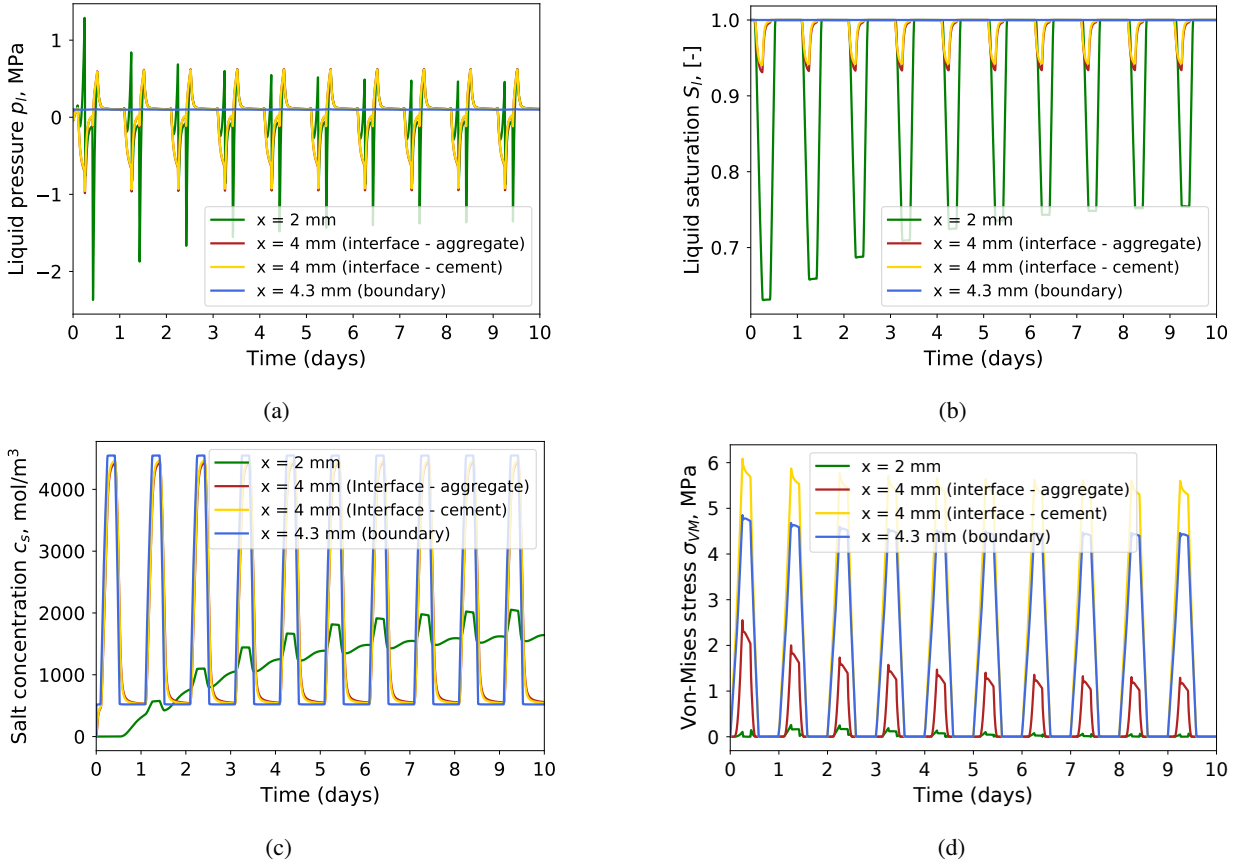


Figure 7: Evolution over 10 freeze-thaw cycles of (a) liquid pressure, (b) liquid saturation, (c) salt concentration and (d) Von Mises stress for the individual aggregate coated with cement paste.

378 will attach to the cement coating. Then, because of the difference in thermal expansion and of the presence of brine
 379 pockets, the ice will stress the cement, which will lead to failure. Since the ITZ in pervious concrete is near the
 380 macrovoid surface, glue spall by the ice could induce significant stresses at the paste/aggregate interface.

381 Given the small thickness of the cement paste coated layer (which is on the order of a few hundred microns), it is
 382 very likely that, after immersion under water, the cement paste becomes saturated very quickly. Consequently, we judge
 383 unlikely the fact that including partial saturation into the model would make it possible to capture the salt pessimum.
 384 We also judge it unlikely because we do not see *a priori* why partial saturation would make salt more detrimental than
 385 in a fully saturated case.

386 3.1.4. Effect of boundary conditions on modeling

387 In the previous sections, we considered that the brine pockets at the boundary are connected so that the salt con-
 388 centration increases when the temperature decreases (see Figure 3). In other words, since the liquid pressure at the
 389 boundary is at atmospheric pressure, the process of cryosuction is not active at the boundary due to the connectivity
 390 of the brine pockets. Eriksson et al. [21] considered two extreme cases: an open boundary to simulate fully connected
 391 brine pockets and a closed boundary to simulate fully isolated brine pockets. A novelty of our study is that we model
 392 and study various connectivity levels. In the present section, to activate the cryosuction at the boundary, we consider
 393 that the brine pockets are isolated and relax the hypothesis that the liquid phase is at atmospheric pressure.

394 We note $p_L^{lowbound}$ the liquid pressure obtained at the system boundary when assuming that ice around the brine
 395 pockets is at atmospheric pressure and that Thomson equation (22) is verified. $p_L^{lowbound}$ is, therefore, the liquid pressure
 396 when the cryosuction is maximum. In such a case, the depression of the liquid at the boundary is equal to $p_L^{lowbound} -$
 397 p_{atm} . In the present section, we consider that only a fraction X of this depression applies, and therefore that the liquid

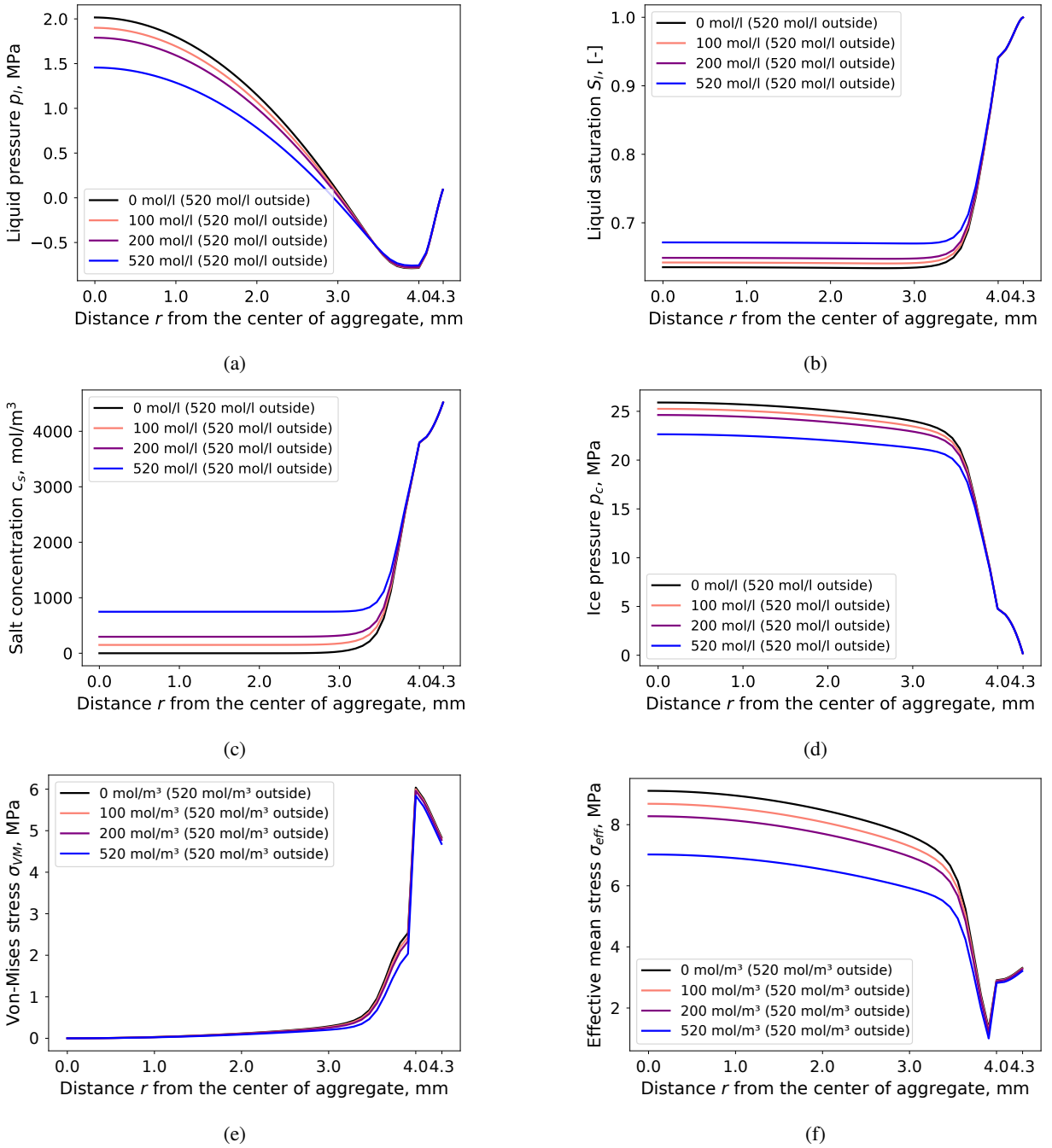


Figure 8: (a) Liquid pressure, (b) liquid saturation, (c) salt concentration, (d) ice pressure, (e) Von Mises stress, and (f) effective mean stress for various initial conditions at $t = 6$ h corresponding to the beginning of the -20 °C plateau for individual aggregate coated with cement paste.

398 pressure p_L at the boundary verifies:

$$p_L - p_{atm} = X (p_L^{lowbound} - p_{atm}) \quad (33)$$

399 The non-connectivity of the brine pockets increases with the magnitude of X . We consider three different fractions.

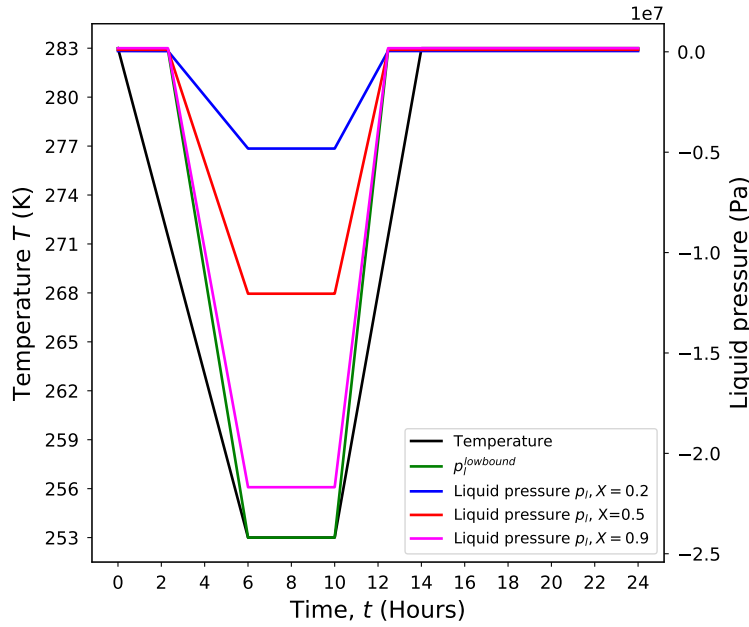


Figure 9: Liquid pressure p_L applied at the boundary for various brine pockets connectivities.

Each fraction is related to the degree of connectivity of the brine pockets at the system boundary. When X is equal to 0, we ensure $p_L = p_{atm}$, which means that the brine pockets are totally connected and that there is no cryosuction at the boundaries, like in the simulations performed in Sections 3.1.1, 3.1.2 and 3.1.3. In the case $X = 1$, the cryosuction is fully active at the boundary and $p_L = p_L^{lowbound}$. Figure 9 represents the liquid pressure at the boundary for $X = 0.2$, $X = 0.5$, and $X = 0.9$. We then use the calculated liquid pressure to solve Equation (22) to obtain the salt concentration at the boundary.

Figure 10 presents the liquid saturation, liquid pressure, salt concentration and Von Mises stress for different brine connectivities ranging from fully connected brine pockets (i.e., $X = 0$ and $p_L = p_{atm}$) to partially connected brine pockets ($X = 0.2$, $X = 0.5$, $X = 0.9$) at $t = 6$ h corresponding to the beginning of the -20 °C plateau. We observe that the less the brine pockets are connected, the lower the salt concentration at the boundary. Therefore, less salt diffuses toward the inside of the material, compared to the case of fully connected brine pockets. We observe low liquid saturation and maximum stresses for the case with a higher non-connectivity degree (i.e., $X = 0.9$). Also, the connectivity of the brine pockets impacts the localization of the maximal stresses. For $X = 0.9$, the maximal stress is at the surface of the cement paste, not in the vicinity of the paste/aggregate interface. We find that the maximal shear stress is located at the interface for the case $X = 0.5$.

We conclude that the hydraulic and salt concentration boundary conditions significantly impact the response of the material subject to freeze-thaw cycles in the presence of salt and saturated conditions. We can speculate that various types of boundary conditions can be present at various locations on the concrete surface. Indeed, some zones at the surface can be in contact with brine pockets, while others can be in contact with pure ice. Experimental work is necessary to fully understand the behavior of the frozen solution at the outer surface of the concrete.

3.1.5. Influence of various material properties on the response to freeze-thaw cycles

In this section, we investigate the impact of various cement paste and aggregate properties. We investigate the impact of porosity, permeability, and coefficient of thermal expansion, for both cement paste and aggregate.

We consider the porosity couples reported in Table 5 to estimate the impact of the porosity of cement paste and aggregates. The other materials parameters are kept unchanged and correspond to the values summarized in Table 3. Figure 11-a presents the resulting Von Mises stress distribution at $t = 6$ h. We find that the porosity does not impact much the Von Mises stress maximal value.

To estimate the impact of the coefficient of thermal expansion of cement and aggregate, we consider the values

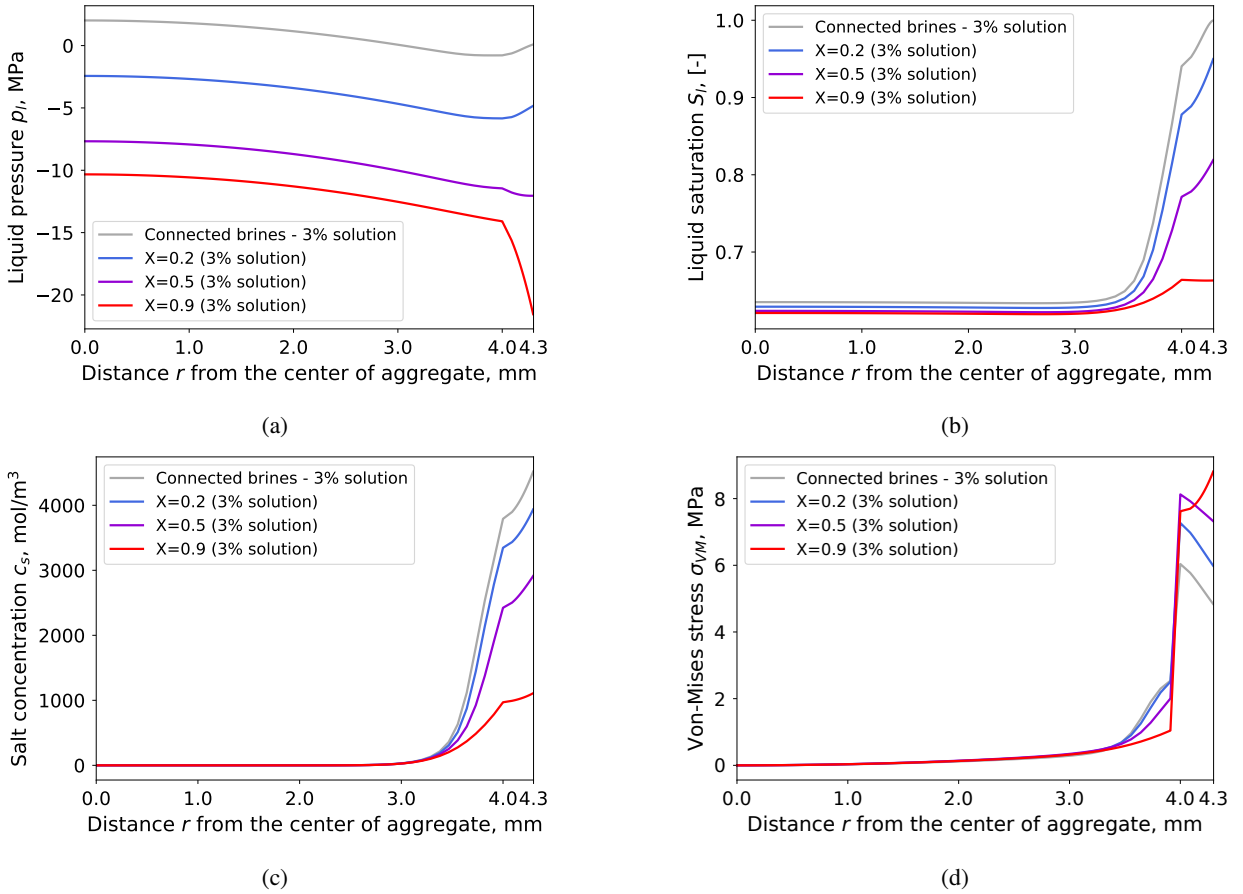


Figure 10: (a) Liquid pressure, (b) liquid saturation, (c) salt concentration and (d) Von Mises stress for various boundary conditions at $t = 6$ h corresponding to the beginning of the -20 °C plateau for individual aggregate coated with cement paste.

428 reported in Table 4. We find (see Figures 11-c and 11-d) that the higher the difference between the coefficient of thermal
 429 expansion of the cement paste and the aggregate, the higher the maximal stress at the interface. The maximal stress does
 430 not depend on those two coefficients independently but on the mismatch between those two coefficients. The magnitude
 431 of the stresses can double when the coefficients of thermal expansion for paste and aggregate span a realistic range.
 432 Consequently, the cement and aggregate dilation mismatch could explain part of the damage that concrete sustains
 433 when subjected to freeze-thaw cycles. Therefore, it might be essential to lower the mismatch between cement paste
 434 and aggregate coefficient of thermal expansion to improve the freeze-thaw durability of pervious concrete.

435 From Figures 11-c and 11-d we also observe that, in the absence of thermal mismatch, the maximal stress at the
 436 interface would be about five times smaller than the thermal mismatch obtained with the material properties given in
 437 Table 3. Consequently, for the pervious concretes here simulated, it appears that stresses are mostly of thermal origin
 438 and that poromechanical effects per se are of second order.

439 We investigate the impact of permeability for the various permeabilities reported in Table 6. We find that the
 440 lower the cement paste permeability, the higher the maximal Von Mises stress, as observed in Figure 11. A low-
 441 permeability cement paste (i.e., a paste with $k_{paste} = 10^{-22}$ m²) exhibits the highest stress at the interface among all
 442 our simulations. The stresses at the interface can increase by a factor of 1.5 when the permeability of cement paste
 443 decreases from $1 \cdot 10^{-21}$ m² to $1 \cdot 10^{-22}$ m². The high permeability of the cement paste allows fast dissipation of
 444 the liquid pore pressure, which dissipates the tensile stresses that might develop. The impact of variations of thermal
 445 expansion coefficient and permeability on the stresses is larger than that of the variations of porosity of the cement
 446 paste and aggregates.

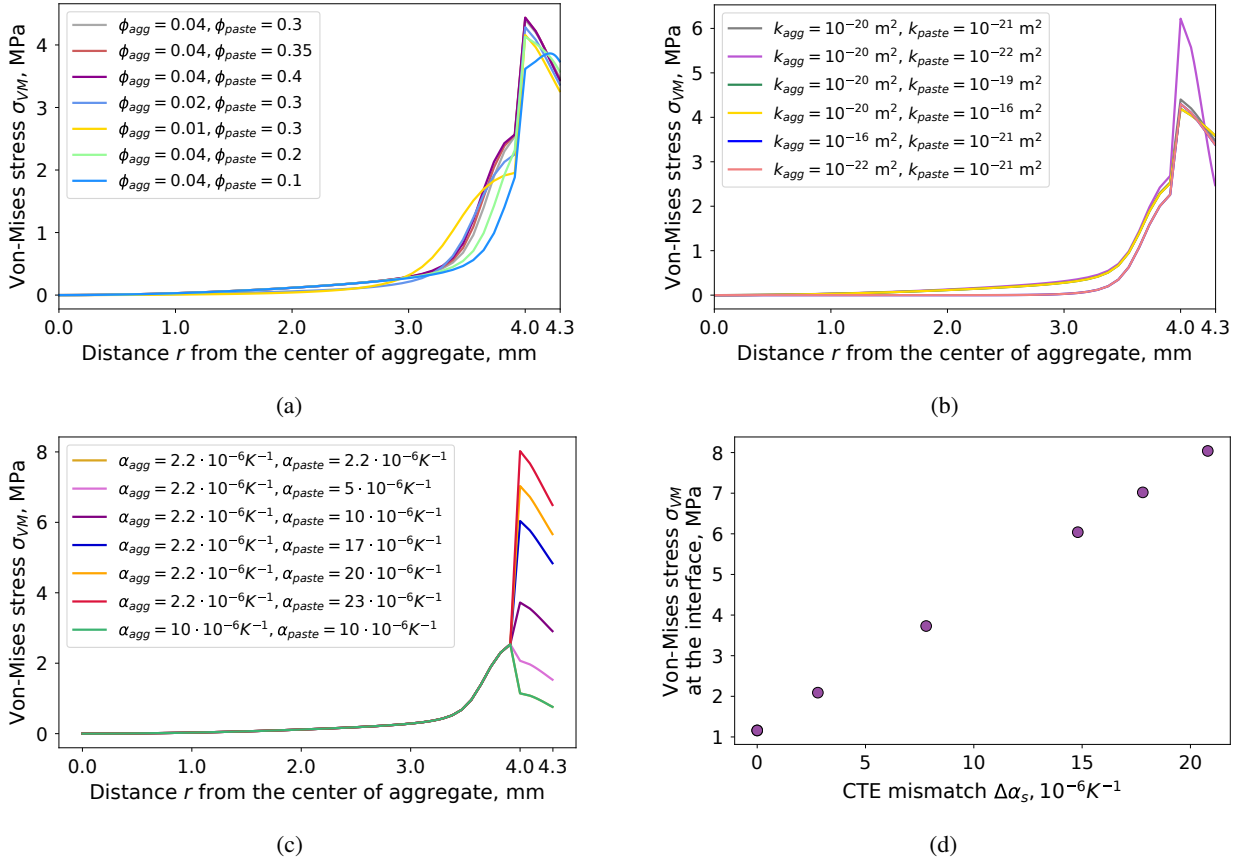


Figure 11: Influence of cement paste and aggregates properties on Von Mises stress (at $t = 6$ h corresponding to the beginning of the -20 °C plateau) for an individual aggregate coated with cement paste: (a) porosity, (b) permeability, (c) coefficient of thermal expansion and, (d) Von Mises stress at the interface as function of coefficient of thermal expansion mismatch.

Coefficient of thermal expansion α		Maximal Von Mises stress at the interface (MPa)
Cement	Aggregate	
$\alpha_{paste} = 17 \cdot 10^{-6} K^{-1}$	$\alpha_{agg} = 2.2 \cdot 10^{-6} K^{-1}$	6.04
$\alpha_{paste} = 10 \cdot 10^{-6} K^{-1}$	$\alpha_{agg} = 10 \cdot 10^{-6} K^{-1}$	1.16
$\alpha_{paste} = 2.2 \cdot 10^{-6} K^{-1}$	$\alpha_{agg} = 2.2 \cdot 10^{-6} K^{-1}$	1.16
$\alpha_{paste} = 23 \cdot 10^{-6} K^{-1}$	$\alpha_{agg} = 2.2 \cdot 10^{-6} K^{-1}$	8.04
$\alpha_{paste} = 20 \cdot 10^{-6} K^{-1}$	$\alpha_{agg} = 2.2 \cdot 10^{-6} K^{-1}$	7.02
$\alpha_{paste} = 10 \cdot 10^{-6} K^{-1}$	$\alpha_{agg} = 2.2 \cdot 10^{-6} K^{-1}$	3.73
$\alpha_{paste} = 5 \cdot 10^{-6} K^{-1}$	$\alpha_{agg} = 2.2 \cdot 10^{-6} K^{-1}$	2.09

Table 4

Coefficients of thermal expansion and resulting maximum stress at the interface for the various parametric simulations.

3.1.6. Influence of the presence of a crack

This section explores the response of the same system as the previous one (i.e., one aggregate coated with cement paste) but in the presence of a crack in the cement paste layer. We presented the geometry of the system in Figure 2. In this case, the system's boundary (on which the boundary conditions are applied) is the outside surface of the cement paste, the crack lips, and the exposed aggregate surface. Mechanically, the crack lips are free from mechanical stress. The temperature, salt concentration, and liquid pressure at the boundary are similar to the boundary conditions used in Section 3.1. Figure 12 shows the mean effective stress and the Von Mises stress at the vicinity of the crack. In the aggregate and the cement paste, both stresses are maximal close to the crack tip. We can attribute this high stress to

Modeling salt-frost damage of pervious concrete

Porosity ϕ		Maximal Von Mises stress at the interface (MPa)
Cement	Aggregate	
$\phi_{paste} = 0.3$	$\phi_{agg} = 0.04$	4.4
$\phi_{paste} = 0.35$	$\phi_{agg} = 0.04$	4.43
$\phi_{paste} = 0.4$	$\phi_{agg} = 0.04$	4.44
$\phi_{paste} = 0.3$	$\phi_{agg} = 0.02$	4.28
$\phi_{paste} = 0.3$	$\phi_{agg} = 0.01$	4.16
$\phi_{paste} = 0.2$	$\phi_{agg} = 0.04$	4.13
$\phi_{paste} = 0.1$	$\phi_{agg} = 0.04$	3.62

Table 5

Porosities and resulting maximum stress at the interface for the various parametric simulations.

Permeability (k)		Maximal Von Mises stress at the interface (MPa)
Cement	Aggregate	
$k_{paste} = 10^{-21} \text{ m}^2$	$k_{agg} = 10^{-20} \text{ m}^2$	4.4
$k_{paste} = 10^{-22} \text{ m}^2$	$k_{agg} = 10^{-20} \text{ m}^2$	6.22
$k_{paste} = 10^{-23} \text{ m}^2$	$k_{agg} = 10^{-20} \text{ m}^2$	19.7
$k_{paste} = 10^{-19} \text{ m}^2$	$k_{agg} = 10^{-20} \text{ m}^2$	4.2
$k_{paste} = 10^{-16} \text{ m}^2$	$k_{agg} = 10^{-20} \text{ m}^2$	4.2
$k_{paste} = 10^{-21} \text{ m}^2$	$k_{agg} = 10^{-16} \text{ m}^2$	4.3
$k_{paste} = 10^{-21} \text{ m}^2$	$k_{agg} = 10^{-22} \text{ m}^2$	4.3

Table 6

Permeabilities and resulting maximum stress at the interface for the various parametric simulations.

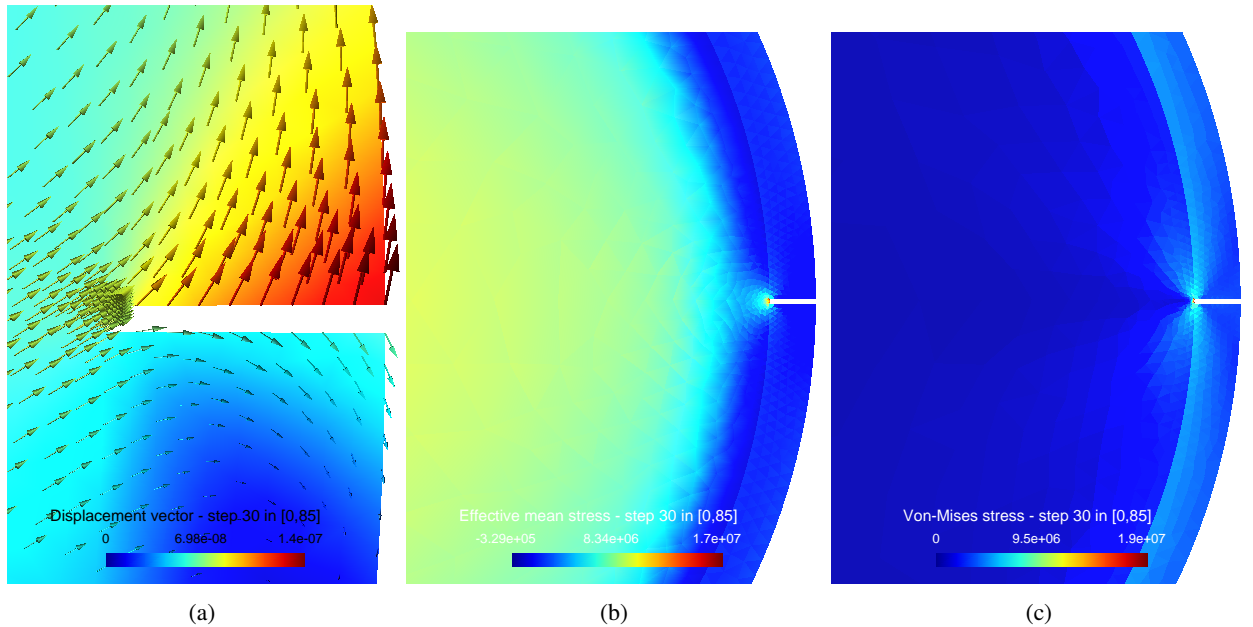


Figure 12: (a) Displacement, (b) effective mean stress and (c) Von Mises stress at $-20 \text{ }^\circ\text{C}$ at 6 h for individual aggregate coated with fractured cement paste.

455 the noticeable difference between the aggregate and cement paste coefficient of thermal expansion. Upon freezing, the
 456 crack opens because the edges of the two cement lips move in opposite directions due to their contraction, as shown
 457 in Figure 12. The stresses in the aggregate and cement paste far from the crack are the same as in the intact system.

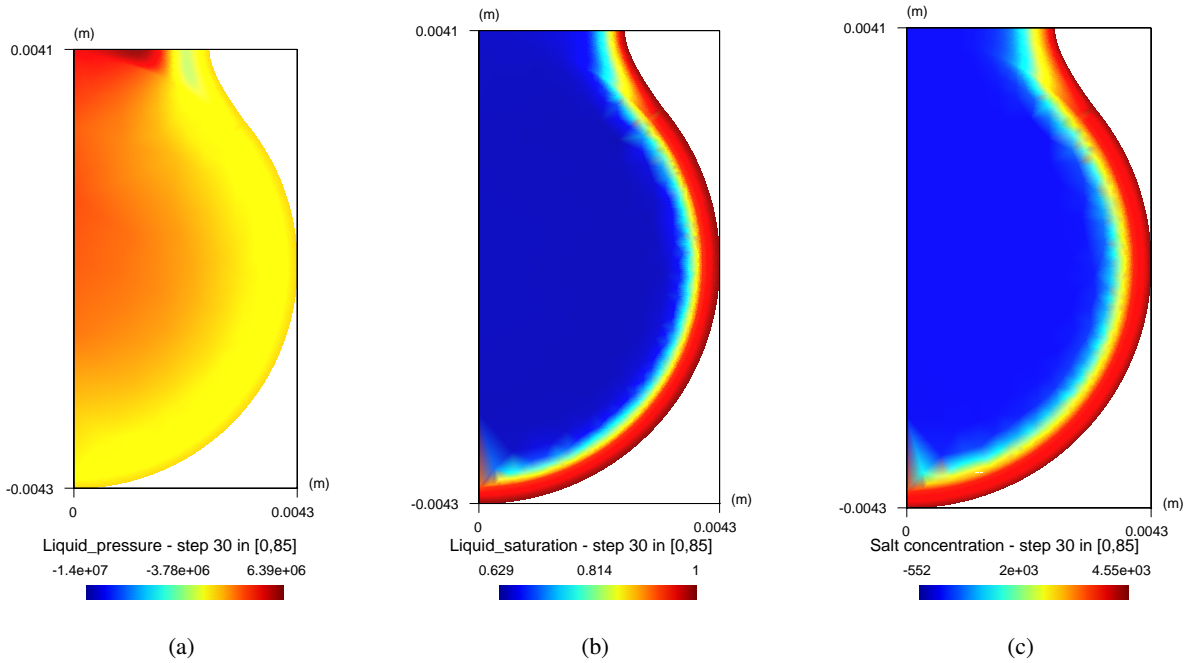


Figure 13: (a) Liquid pressure, (b) liquid saturation, and (c) salt concentration at $-20\text{ }^{\circ}\text{C}$ at 6 h for two aggregates coated and bonded with cement paste.

3.2. System of two cemented aggregates

This section aims to study a more complex geometry consisting of two aggregates coated and bonded with cement paste. This geometry aims at modeling the behavior of pervious concrete at the level of its constituents by considering the mechanical interaction between the aggregates and the cement that binds and coats them. In this section, we limit the study to the case of connected brine pockets (see Section 3.1.4 for the impact on boundary conditions). We summarize the value of materials parameters in Table 3. Figure 2-b displays the simulated geometry.

3.2.1. Qualitative description of the response to 1 freeze-thaw cycle

Simulations show that temperature varies almost homogeneously in the system: indeed, at all times, the temperature everywhere differs at maximum by $0.01\text{ }^{\circ}\text{C}$ from the temperature imposed on the edges.

We focus on the mechanical response of this system to the freeze-thaw solicitation. Figure 13 shows the liquid pressure, liquid saturation, and salt concentration at $t = 6\text{ h}$. Figure 14 shows the Von Mises stress in the system at various times. Around $t = 10\text{ h}$, at which time the temperature reached its minimal value $T = -20\text{ }^{\circ}\text{C}$, the Von Mises stress is maximal at the level of the contact between the two aggregates. The fact that the aggregates block the cement paste deformation due to their different coefficients of thermal expansion could explain the high shear stress in this contact region. Moreover, we also observe significant shear stresses at the interface between aggregates and cement paste, but those shear stresses remain small compared to the stresses developed in the contact region.

Figure 15 displays the effective mean stress $\sigma_m^{eff} = \sigma_m + S_{LPL} + S_{CPC}$ in the system at various times in the freezing process. The figure shows that significant tensile stresses prevail at the aggregate center. The fact that the drainage length in the cement paste is larger for water in the contact region than outside the contact region could explain the tensile stresses prevailing in the contact region. The stresses start decreasing after they have reached a maximum value, between 8 h to 10 h after the beginning of the cycle, when the temperature has reached $-20\text{ }^{\circ}\text{C}$. The decrease is due to water flowing to the outside boundary, as we observed for one aggregate coated with a cement paste layer. The combined effect of the Von Mises stress and mean effective stress will be discussed later in the paper by using the Drucker-Prager criterion.

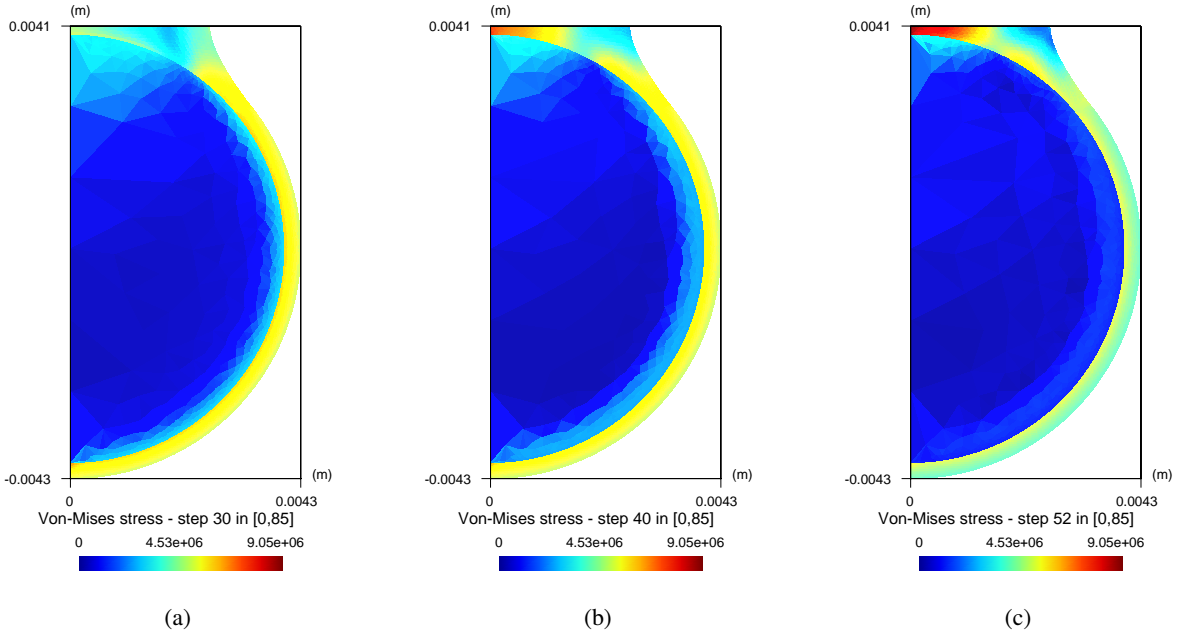


Figure 14: Von Mises stress for two aggregates coated and bonded with cement paste at $-20\text{ }^{\circ}\text{C}$ at (a) 6 h, (b) 8 h, and (c) 10 h.

3.2.2. Influence of coefficients of thermal expansion on response to freeze-thaw cycle

482 In this section, we study the impact of the coefficients of thermal expansion on the behavior of the two aggregates
 483 coated and bonded with cement paste. Figure 16 shows that the larger the difference between the coefficient of thermal
 484 expansion of aggregates and cement paste, the larger the stress developed in the contact region between the two
 485 aggregates and at the paste/aggregate interface. The stress is maximal for the simulations with the largest mismatch of
 486 coefficients of thermal expansion. In Figure 16b we present the stress for a system with equal coefficient of thermal
 487 expansion for the cement paste and the aggregates. We notice that the shear stresses are much lower than in the case
 488 of mismatch, with maximal shear stresses in the contact region and the aggregate. The trends observed on the system
 489 made of two aggregates concerning thermal mismatch are consistent with those observed on the system made of one
 490 aggregate and discussed in Section 3.1.5.
 491

3.3. Identification of regions where damage is most likely to occur

492 This section introduces failure criteria to predict whether, upon freezing, the materials are susceptible to get dam-
 493 aged. This approach allows us also to identify the regions where damage is most likely to occur. We consider a
 494 Mohr-Coulomb criterion for the interface and a Drucker-Prager criterion for cement paste and the aggregates, as al-
 495 ready mentioned in Section 2.5. The parameters for the two criteria are in Table 3.
 496

3.3.1. Interface

497 Figure 17 displays the quantity $|\tau| - (\sigma_{rr} + S_L p_L + S_C p_C) \tan(\theta)$, which is homogeneous to a stress, at the interface.
 498 If this quantity is larger than the cohesion of the interface, failure should occur. The zone where damage is likely to
 499 occur is the interface close to the contact region between the two aggregates. The interface must have a cohesion larger
 500 than 9 MPa to avoid failure for the chosen materials and freezing conditions. This value is very large for paste/aggregate
 501 interfaces. Indeed, Jebli et al. [62] report a cohesion of 3 MPa for the paste/aggregate interface.
 502

503 Using a poromechanical model, Rahman and Grasley [18] showed that high tensile stresses develop at the ITZ be-
 504 cause of the mismatch of coefficient of thermal expansion between the aggregate and the matrix. Callan [63] obtained
 505 similar results. Cwirzen and Pentala [64] showed experimentally that the ITZ properties govern the damage process
 506 under salt-frost attacks of non-air-entrained high-performance concretes. Therefore, enhancing the cement paste dura-
 507 bility without enhancing the paste/aggregate interface durability may be insufficient to enhance concrete durability
 508 since the interface plays a significant role.

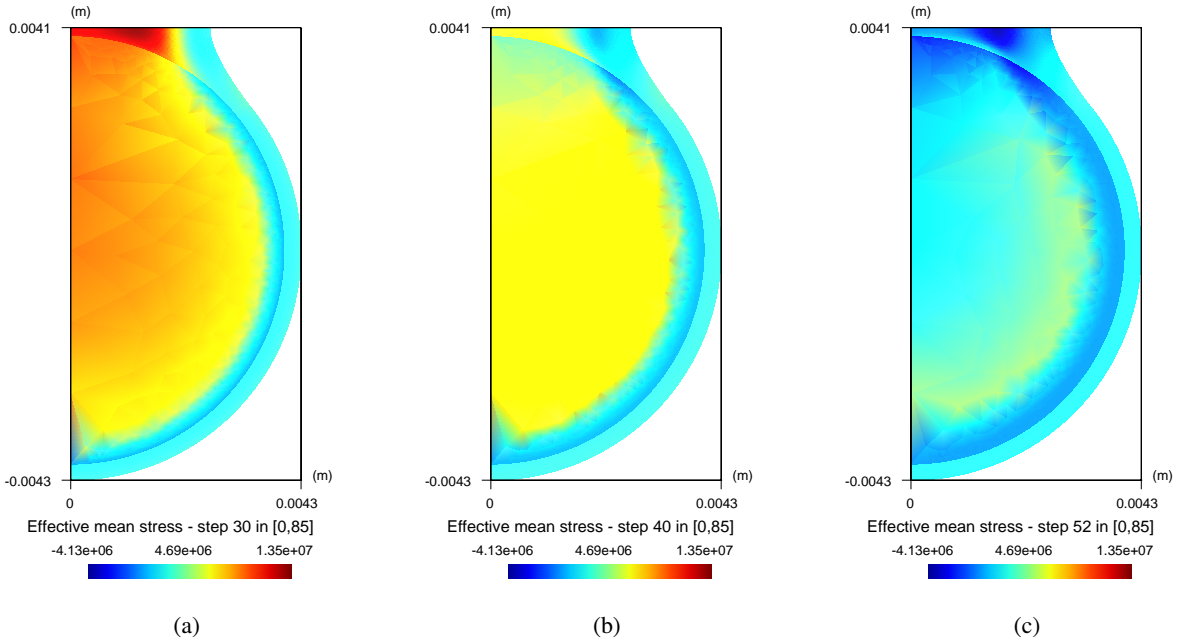


Figure 15: Effective mean stress for two aggregates coated and bonded with cement paste at $-20\text{ }^{\circ}\text{C}$ at (a) 6 h, (b) 8 h, and (c) 10 h.

509 3.3.2. Aggregate and cement paste

510 We now study damage in the aggregate and the cement paste by considering a Drucker-Prager failure model for
 511 those two phases. Figure 18 presents the value of the quantity $B\sigma_m^{eff} + \sigma_{VM}$, which is homogeneous to a stress, in
 512 the aggregates and the coating cement paste, for the system made of two aggregates coated and bonded with cement
 513 paste. Failure could occur if this quantity is larger than the considered Drucker-Prager material parameter A , which is
 514 related to the cohesion of the material. In other words, to avoid damage in the cement paste, we need to ensure that
 515 $A > B\sigma_m^{eff} + \sigma_{VM}$. From Figure 18, we conclude that, in the cement paste and the aggregates, failure is the most
 516 likely to occur in the contact region between the aggregates.

517 3.3.3. Comparison of modeling results with experiments from literature

518 Experimentally, having a weak paste/aggregate cohesion will result in failure at the level of the interface. In the
 519 recent work by Song et al. [65], the authors study the role of the interface transitional zone in pervious concrete
 520 during freeze-thaw cycles in the presence of salt. Using SEM analysis, the authors show that the main cause of
 521 damage is the interface debonding during the freeze-thaw cycles. Our model provides results in accordance with these
 522 observations, as it shows the significant role of the paste/aggregate interface properties. Song et al. [65] also explain
 523 that an inconsistency between the deformations of aggregate and cement paste is a critical mechanism of damage.
 524 Callan [63] showed that high tensile stress at the ITZ is developed due to the mismatch of coefficient of thermal
 525 expansion between the aggregate and the matrix. Our model is also consistent with this observation, as we show that
 526 the mismatch in thermal dilation coefficient can lead to significant stresses at the interface.

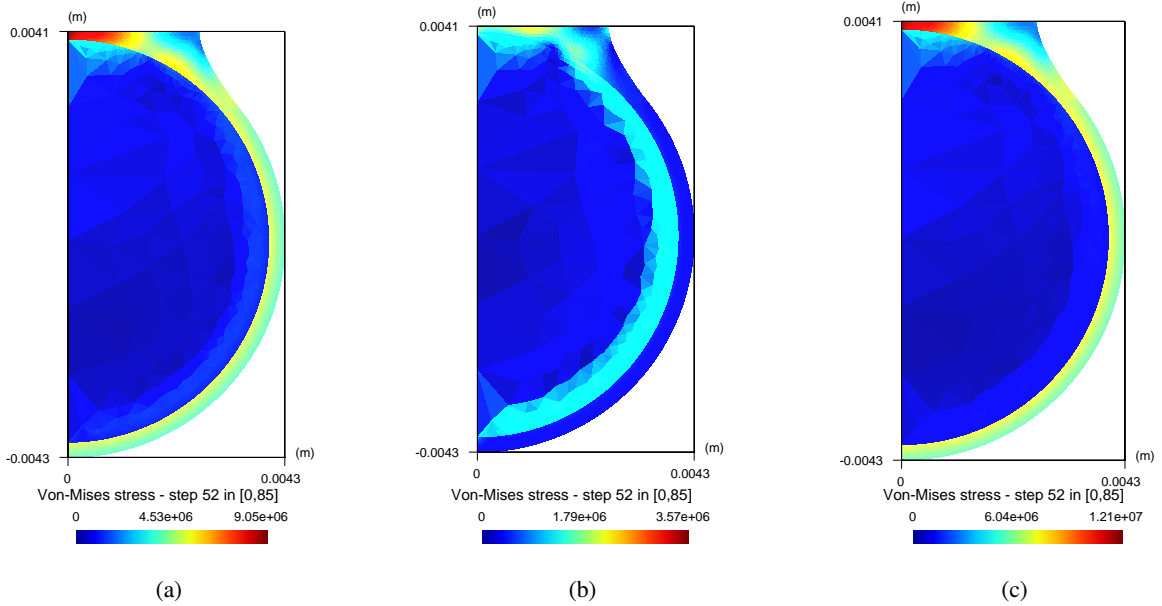


Figure 16: Von Mises stress for two aggregates coated and bonded with cement paste at $-20\text{ }^{\circ}\text{C}$ (6 h) for various coefficients of thermal expansion. (a) Case 1: $\alpha_{agg} = 2.2 \cdot 10^{-6}\text{ K}^{-1}$ and $\alpha_{paste} = 17 \cdot 10^{-6}\text{ K}^{-1}$. (b) Case 2: $\alpha_{agg} = 10 \cdot 10^{-6}\text{ K}^{-1}$ and $\alpha_{paste} = 10 \cdot 10^{-6}\text{ K}^{-1}$. (c) Case 3: $\alpha_{agg} = 2.2 \cdot 10^{-6}\text{ K}^{-1}$ and $\alpha_{paste} = 23 \cdot 10^{-6}\text{ K}^{-1}$.

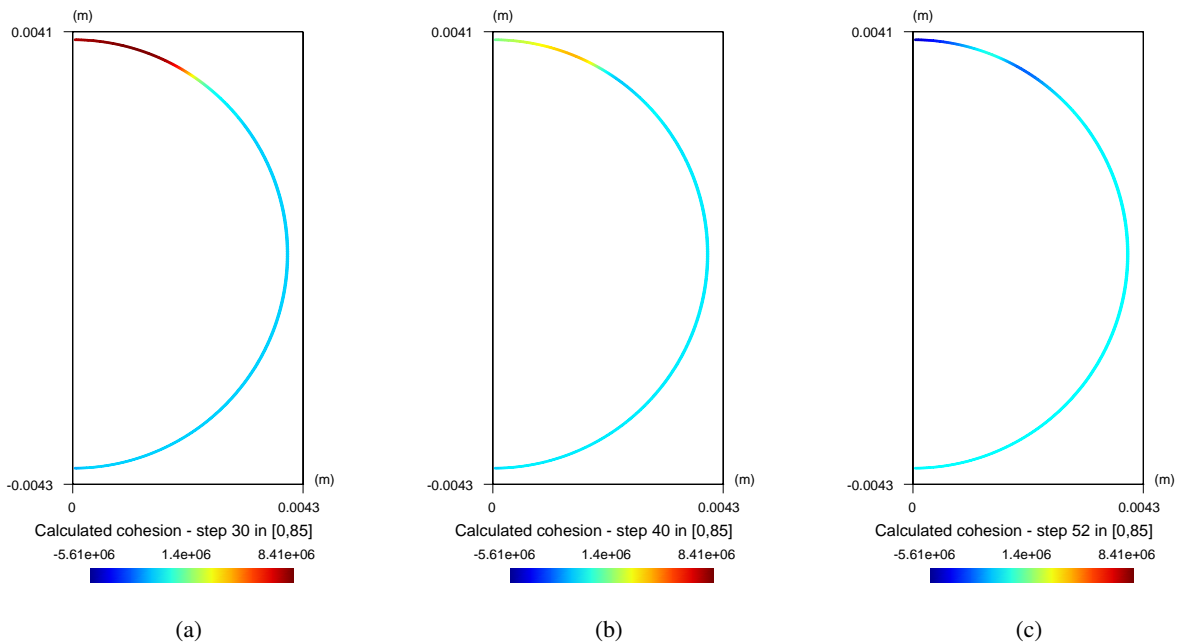


Figure 17: Quantity $|\tau| - \sigma_{rr} \tan(\theta)$ at $-20\text{ }^{\circ}\text{C}$ at (a) 6 h, (b) 8 h, and (c) 10 h for two aggregates coated and bonded with cement paste.

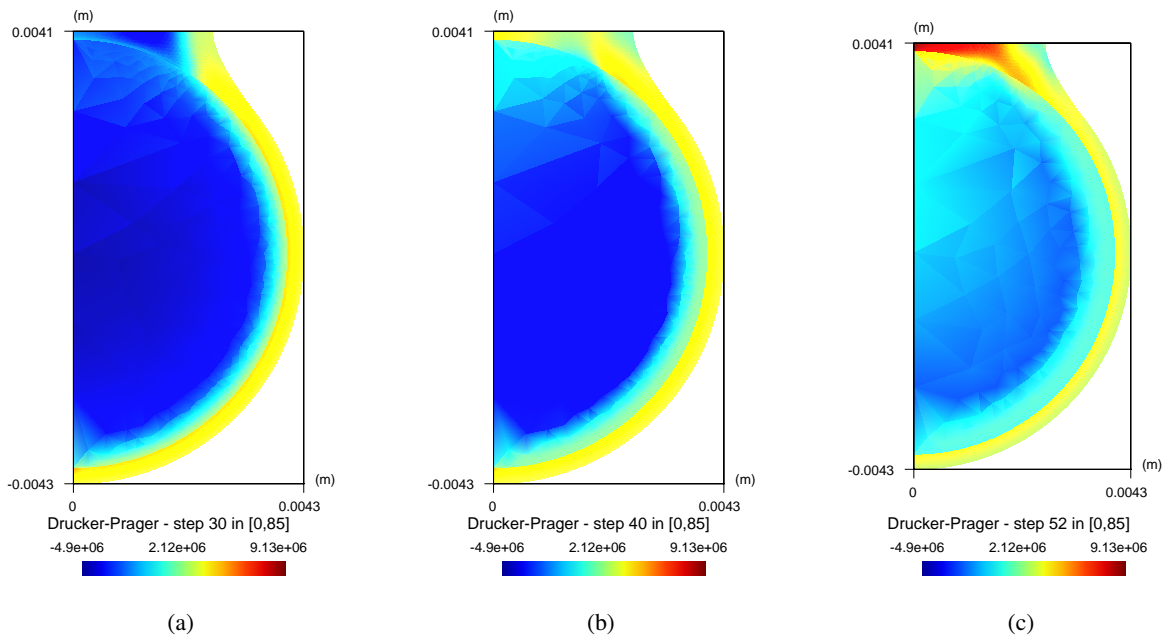


Figure 18: Quantity $B\sigma_m^{eff} + \sigma_{VM}$ at $-20\text{ }^\circ\text{C}$ at (a) 6 h, (b) 8 h, and (c) 10 h for two aggregates coated and bonded with cement paste.

4. Conclusions

We developed a poromechanical model to simulate the freezing of porous solids in saturated conditions and in the presence of dissolved salts. We used this poromechanical approach to gain insight into the damage of pervious concrete at the level of a few aggregates coated and bonded with cement paste. We used the model to calculate the stresses and ice saturation distributions in various systems with various boundary conditions, upon freeze-thaw cycles, in the presence of deicing salts. Based on the various simulations presented earlier in the manuscript, the most important conclusions of this work are:

- Significant tensile effective stresses prevail in the center of the aggregates upon freezing because of the crystallization of significant volume fractions of ice.
- Significant shear stresses develop within the cement paste upon freezing. They reach a maximum value at the paste/aggregate interface and in the contact zone between aggregates.
- These stresses could exceed the strength of cement paste and the aggregates, inducing damage during the repeated freeze-thaw cycles. Such damage is the most likely to occur at the paste/aggregate interface or in the contact zone between two aggregates.
- Salt accumulates in the material over repeated freeze-thaw cycles and therefore makes the shear stresses in the cement paste layer decrease with the number of cycles. We cannot retrieve a salt pessimum with the physical ingredients implemented in the model, although several observed this pessimum experimentally. This inability shows that we must find the physical reason for this salt pessimum elsewhere.
- The shear stresses within the cement paste layer depend significantly on the mismatch between the coefficients of thermal expansion of the cement paste and the aggregate. The magnitude of those stresses can double when those coefficients for cement paste and aggregates span a realistic range. For the pervious concretes here modeled and the conditions considered, thermomechanical effects are more significant than poromechanical effects. Therefore, designing pervious concrete mixtures with a minimized mismatch of coefficient of thermal expansion could prove an efficient way to improve the freeze-thaw durability of pervious concrete.
- The shear stresses within the cement paste layer depend significantly on the cement paste permeability also. Those stresses can increase by a factor of 1.5 when the cement paste permeability decreases from $1 \cdot 10^{-21} \text{ m}^2$ to $1 \cdot 10^{-22} \text{ m}^2$.
- The porosity of the cement paste has a much smaller impact on the magnitude of stresses generated during freeze-thaw than the coefficient of thermal expansion or the permeability.
- The ice brine mixture, formed at the surface of the cement paste upon freezing, is composed of ice and brine pockets more or less interconnected. The degree of connectivity of such brine pockets significantly impacts the stresses generated in the cement paste. Larger connectivity generates lower stresses than those obtained with a lower degree of connectivity.
- If the layer of cement paste has cracked, significant stresses are generated at the crack during freezing because of the contraction of the two cement lips in opposite directions.
- Enhancing the cement paste durability without enhancing the durability of the paste/aggregate interface may not be sufficient to improve the concrete durability, as the impact of the paste/aggregate interface on the concrete durability is significant.

The model developed in the present work makes it possible to calculate the stresses in cement-based materials, particularly pervious concrete, under frost attacks. This model can help quantify the stress states under various conditions. It can also orient reflections on materials properties to design concretes that resist better frost attacks in the presence of deicing salt. However, we should improve the model by considering incorporating glue-spall to explain the experimentally observed salt pessimum. Also, to quantitatively assess the impact of repeated freeze-thaw cycles, it is necessary to implement a damage model that considers the decay of the resistance of the aggregates, the cement paste, and their interface. Moreover, including the interfacial transition zone (ITZ) in the simulations could be interesting to

572 assess its impact on the system properties and damage patterns. One could employ the model to simulate more realis-
573 tic geometries in three dimensions to consider more complex geometries involving more than two aggregates. Since,
574 using finite-elements method would be numerically very costly, we propose to identify the damage mechanism and
575 the evolution of the contact between aggregates using FEM. Then, it is possible to envision coarse-grained methods,
576 such as Discrete Elements Method (DEM), to perform simulation yielding macroscopic properties. Furthermore, such
577 simulations will make it possible to compare our modeling results with experimental data such as strength measure-
578 ments (e.g., by uniaxial compression) or stiffness measurements (e.g., by ultrasounds). Such upscaling could be done
579 numerically for instance, by using DEM modeling, in which the contact law between the discrete elements (i.e., the
580 aggregates) would be fitted on the results from our present finite element calculations.

References

- 581
- 582 [1] Schaefer, V. R., Wang, K., Kevern, J. T., and Suleiman, M. T. Mix design development for pervious concrete in cold weather climates. <https://rosap.nrl.bts.gov/view/dot/38663>, 2006.
- 583
- 584 [2] Chandrappa, A. K. and Biligiri, K. P. Pervious concrete as a sustainable pavement material – Research findings and future prospects: A state-of-the-art review. *Construction and Building Materials*, 111:262–274, May 2016. ISSN 0950-0618. doi: 10.1016/j.conbuildmat.2016.02.054.
- 585
- 586 [3] Xie, X., Zhang, T., Yang, Y., Lin, Z., Wei, J., and Yu, Q. Maximum paste coating thickness without voids clogging of pervious concrete and its relationship to the rheological properties of cement paste. *Construction and Building Materials*, 168:732–746, April 2018. ISSN 0950-0618. doi: 10.1016/j.conbuildmat.2018.02.128.
- 587
- 588
- 589 [4] Cutler, H. E., Wang, K., Schaefer, V. R., and Kevern, J. T. Resistance of Portland cement pervious concrete to deicing chemicals. *Transportation Research Record*, 2164(1):98–104, January 2010. ISSN 0361-1981. doi: 10.3141/2164-13.
- 590
- 591 [5] Vancura, M., MacDonald, K., and Khazanovich, L. Microscopic analysis of paste and aggregate distresses in pervious concrete in a wet, hard freeze climate. *Cement and Concrete Composites*, 33(10):1080–1085, November 2011. ISSN 0958-9465. doi: 10.1016/j.cemconcomp.2011.05.011.
- 592
- 593
- 594 [6] Wu, H., Liu, Z., Sun, B., and Yin, J. Experimental investigation on freeze–thaw durability of Portland cement pervious concrete (PCPC). *Construction and Building Materials*, 117:63–71, August 2016. ISSN 0950-0618. doi: 10.1016/j.conbuildmat.2016.04.130.
- 595
- 596 [7] Liu, H., Luo, G., Wei, H., and Yu, H. Strength, permeability, and freeze–thaw durability of pervious concrete with different aggregate sizes, porosities, and water–binder ratios. *Applied Sciences*, 8(8):1217, August 2018. doi: 10.3390/app8081217.
- 597
- 598 [8] Kevern J. T. and Schaefer V. R. Effect of coarse aggregate on the freeze–thaw durability of pervious concrete. *Journal of Materials in Civil Engineering*, 22(5):469–475, May 2010. doi: 10.1061/(ASCE)MT.1943-5533.0000049.
- 599
- 600 [9] Zhong, R. and Wille, K. Material design and characterization of high performance pervious concrete. *Construction and Building Materials*, 98:51–60, November 2015. ISSN 0950-0618. doi: 10.1016/j.conbuildmat.2015.08.027.
- 601
- 602 [10] Pigeon, M., Marchand, J., and Pleau, R. Frost resistant concrete. *Construction and Building Materials*, 10(5):339–348, July 1996. ISSN 0950-0618. doi: 10.1016/0950-0618(95)00067-4.
- 603
- 604 [11] Powers, T. C. Resistance of concrete to frost at early ages. *Portland Cement Assoc R & D Lab Bull*, (No 71), 1956.
- 605
- 606 [12] Valenza, J. J. and Scherer, G. W. Mechanism for Salt Scaling. *Journal of the American Ceramic Society*, 89(4):1161–1179, 2006. ISSN 1551-2916. doi: 10.1111/j.1551-2916.2006.00913.x.
- 607
- 608 [13] Verbeck, G. J. and Klieger, P. Studies of salt scaling of concrete. *Highway Research Board Bulletin*, (150), 1957.
- 609
- 610 [14] Lindmark, S. *Mechanisms of Salt Frost Scaling of Portland Cement-Bound Materials: Studies and Hypothesis*. PhD thesis, Lund University, 1998.
- 611
- 612 [15] Yener, E. A new frost salt scaling mechanism for concrete pavements based on brine rejection from ice layer adhered to concrete surface. *Road Materials and Pavement Design*, 16(1):89–100, January 2015. ISSN 1468-0629. doi: 10.1080/14680629.2014.975153.
- 613
- 614 [16] Zeng, Q., Fen-Chong, T., Dangla, P., and Li, K. A study of freezing behavior of cementitious materials by poromechanical approach. *International Journal of Solids and Structures*, 48(22):3267–3273, November 2011. ISSN 0020-7683. doi: 10.1016/j.ijsolstr.2011.07.018.
- 615
- 616 [17] Coussy, O. Poromechanics of freezing materials. *Journal of the Mechanics and Physics of Solids*, 53(8):1689–1718, August 2005. ISSN 0022-5096. doi: 10.1016/j.jmps.2005.04.001.
- 617
- 618 [18] Rahman, S. and Grasley, Z. A poromechanical model of freezing concrete to elucidate damage mechanisms associated with substandard aggregates. *Cement and Concrete Research*, 55:88–101, January 2014. ISSN 0008-8846. doi: 10.1016/j.cemconres.2013.10.001.
- 619
- 620 [19] Coussy, O. Poromechanics of freezing materials. *Journal of the Mechanics and Physics of Solids*, 53(8):1689–1718, August 2005. ISSN 0022-5096. doi: 10.1016/j.jmps.2005.04.001.
- 621
- 622 [20] Eriksson, D., Gasch, T., Malm, R., and Ansell, A. Freezing of partially saturated air-entrained concrete: A multiphase description of the hygro-thermo-mechanical behaviour. *International Journal of Solids and Structures*, 152-153:294–304, November 2018. ISSN 0020-7683. doi: 10.1016/j.ijsolstr.2018.07.004.
- 623
- 624 [21] Eriksson, D., Wahlblom, D., Malm, R., and Fridh, K. Hygro-thermo-mechanical modeling of partially saturated air-entrained concrete containing dissolved salt and exposed to freeze-thaw cycles. *Cement and Concrete Research*, 141:106314, March 2021. ISSN 0008-8846. doi: 10.1016/j.cemconres.2020.106314.
- 625
- 626 [22] Rhardane, A., Al Haj Sleiman, S., Alam, S. Y., and Grondin, F. A quantitative assessment of the parameters involved in the freeze–thaw damage of cement-based materials through numerical modelling. *Construction and Building Materials*, 272:121838, February 2021. ISSN 0950-0618. doi: 10.1016/j.conbuildmat.2020.121838.
- 627
- 628 [23] Coussy, O. Deformation and stress from in-pore drying-induced crystallization of salt. *Journal of the Mechanics and Physics of Solids*, 54(8):1517–1547, August 2006. ISSN 0022-5096. doi: 10.1016/j.jmps.2006.03.002.
- 629
- 630 [24] Coussy, O. *Poromechanics*. John Wiley & Sons, March 2004. ISBN 978-0-470-09270-5.
- 631
- 632 [25] Coussy, O. *Mechanics and Physics of Porous Solids*. John Wiley & Sons, June 2011. ISBN 978-1-119-95616-7.
- 633
- 634 [26] Lide, D. R. *CRC Handbook of Chemistry and Physics, 85th Edition*. CRC Press. ISBN 978-0-8493-0485-9.
- 635
- 636 [27] Speedy, R. J. Thermodynamic properties of supercooled water at 1 atm. 91(12):3354–3358. ISSN 0022-3654. doi: 10.1021/j100296a049. URL <https://doi.org/10.1021/j100296a049>.
- 637
- 638 [28] Millero, F. J. The apparent and partial molal volume of aqueous sodium chloride solutions at various temperatures. *The Journal of Physical Chemistry*, 74(2):356–362, January 1970. ISSN 0022-3654. doi: 10.1021/j100697a022.
- 639
- 640 [29] Marcus, Y. The standard partial molar volumes of ions in solution. part 4. ionic volumes in water at 0–100 °C. 113(30):10285–10291. ISSN 1520-6106. doi: 10.1021/jp9027244. URL <https://doi.org/10.1021/jp9027244>. Publisher: American Chemical Society.
- 641
- 642 [30] Fabbri, A., Coussy, O., Fen-Chong, T., and Monteiro, P. J. Are deicing salts necessary to promote scaling in concrete? 134(7):589.
- 643 [31] Hashin, Z. and Shtrikman, S. A variational approach to the theory of the effective magnetic permeability of multiphase materials. *Journal of Applied Physics*, 33(10):3125–3131, October 1962. ISSN 0021-8979. doi: 10.1063/1.1728579.
- [32] Lin, C.-I. and Lee, L.-S. A two-ionic-parameter approach for ion activity coefficients of aqueous electrolyte solutions. *Fluid Phase Equilibria*,

- 205(1):69–88, March 2003. ISSN 0378-3812. doi: 10.1016/S0378-3812(02)00275-3.
- [33] Lin, H.-y. and Lee, L.-s. Estimations of activity coefficients of constituent ions in aqueous electrolyte solutions with the two-ionic-parameter approach. *Fluid Phase Equilibria*, 237(1):1–8, October 2005. ISSN 0378-3812. doi: 10.1016/j.fluid.2005.08.005.
- [34] van Genuchten, M. T. A closed-form equation for predicting the hydraulic conductivity of unsaturated soils. *Soil Science Society of America Journal*, 44(5):892–898, 1980. ISSN 1435-0661. doi: 10.2136/sssaj1980.03615995004400050002x.
- [35] Mualem, Y. A new model for predicting the hydraulic conductivity of unsaturated porous media. *Water Resources Research*, 12(3):513–522, 1976. ISSN 1944-7973. doi: 10.1029/WR012i003p00513.
- [36] Dangla, P. Bil-2.6 A modeling platform based on finite volume/element methods. Zenodo, September 2018.
- [37] Geuzaine, C. and Remacle, J.-F. Gmsh: A 3-D finite element mesh generator with built-in pre- and post-processing facilities. *International Journal for Numerical Methods in Engineering*, 79(11):1309–1331, 2009. ISSN 1097-0207. doi: 10.1002/nme.2579.
- [38] Pichler, B. and Hellmich, C. Upscaling quasi-brittle strength of cement paste and mortar: A multi-scale engineering mechanics model. *Cement and Concrete Research*, 41(5):467–476, May 2011. ISSN 0008-8846. doi: 10.1016/j.cemconres.2011.01.010.
- [39] Grasley, Z. C. and Lange, D. A. Thermal dilation and internal relative humidity of hardened cement paste. *Materials and Structures*, 40(3):311–317, April 2007. ISSN 1871-6873. doi: 10.1617/s11527-006-9108-x.
- [40] Meyers, S. L. Thermal expansion characteristics of hardened cement paste and of concrete. *Highway Research Board Proceedings*, 30, 1951.
- [41] Meyers, S. L. Thermal coefficient of expansion of Portland cement—Long time tests. *Industrial & Engineering Chemistry*, 32(8):1107–1112, August 1940. ISSN 0019-7866. doi: 10.1021/ie50368a018.
- [42] Cui, L. and Cahyadi, J. H. Permeability and pore structure of OPC paste. *Cement and Concrete Research*, 31(2):277–282, February 2001. ISSN 0008-8846. doi: 10.1016/S0008-8846(00)00474-9.
- [43] Xu, Y. and Chung, D. D. L. Effect of sand addition on the specific heat and thermal conductivity of cement. *Cement and Concrete Research*, 30(1):59–61, January 2000. ISSN 0008-8846. doi: 10.1016/S0008-8846(99)00206-9.
- [44] Al-Shayea, N. A. Effects of testing methods and conditions on the elastic properties of limestone rock. *Engineering Geology*, 74(1):139–156, July 2004. ISSN 0013-7952. doi: 10.1016/j.enggeo.2004.03.007.
- [45] Aurangzeb, Khan, L. A., and Maqsood, A. Prediction of effective thermal conductivity of porous consolidated media as a function of temperature: A test example of limestones. *Journal of Physics D: Applied Physics*, 40(16):4953–4958, August 2007. ISSN 0022-3727. doi: 10.1088/0022-3727/40/16/030.
- [46] Iscan, A. G., K ok, M. V., and Bagci, A. S. Estimation of permeability and rock mechanical properties of limestone reservoir rocks under stress conditions by strain gauge. *Journal of Petroleum Science and Engineering*, 53(1):13–24, August 2006. ISSN 0920-4105. doi: 10.1016/j.petrol.2006.01.008.
- [47] Selvadurai, A. P. S. and Głowacki, A. Estimates for the local permeability of the Cobourg limestone. *Journal of Rock Mechanics and Geotechnical Engineering*, 10(6):1009–1019, December 2018. ISSN 1674-7755. doi: 10.1016/j.jrmge.2018.07.002.
- [48] Kim, K.-H., Jeon, S.-E., Kim, J.-K., and Yang, S. An experimental study on thermal conductivity of concrete. *Cement and Concrete Research*, 33(3):363–371, March 2003. ISSN 0008-8846. doi: 10.1016/S0008-8846(02)00965-1.
- [49] Mukhopadhyay, A. K., Neekhra, S., and Zollinger, D. G. Preliminary characterization of aggregate coefficient of thermal expansion and gradation for paving concrete. (FHWA/TX-05/0-1700-5), January 2007.
- [50] Ghabezloo, S. Association of macroscopic laboratory testing and micromechanics modelling for the evaluation of the poroelastic parameters of a hardened cement paste. *Cement and Concrete Research*, 40(8):1197–1210, August 2010. ISSN 0008-8846. doi: 10.1016/j.cemconres.2010.03.016.
- [51] Xu, Y. and Chung, D. D. L. Effect of sand addition on the specific heat and thermal conductivity of cement. *Cement and Concrete Research*, 30(1):59–61, January 2000. ISSN 0008-8846. doi: 10.1016/S0008-8846(99)00206-9.
- [52] Nguyen, T. Q. *Physicochemical modelling of chloride ingress into cementitious materials*. PhD thesis, Ecole des Ponts, ParisTech, 2007.
- [53] Yang, J., Cai, X., Pang, Q., Guo, X.-w., Wu, Y.-l., and Zhao, J.-l. Experimental study on the shear strength of cement-sand-gravel material. <https://www.hindawi.com/journals/amse/2018/2531642/>, June 2018. ISSN 1687-8434.
- [54] Gu, X., Hong, L., Wang, Z., and Lin, F. Experimental study and application of mechanical properties for the interface between cobblestone aggregate and mortar in concrete. *Construction and Building Materials*, 46:156–166, September 2013. ISSN 0950-0618. doi: 10.1016/j.conbuildmat.2013.04.028.
- [55]  ztekin, E., Pul, S., and H sem, M. Experimental determination of Drucker-Prager yield criterion parameters for normal and high strength concretes under triaxial compression. *Construction and Building Materials*, 112:725–732, June 2016. ISSN 0950-0618. doi: 10.1016/j.conbuildmat.2016.02.127.
- [56] Taylor, M. A. and Brooms, B. B. Shear bond strength between coarse aggregate and cement paste or mortar. *Journal Proceedings*, 61(8):939–958, August 1964. ISSN 0002-8061. doi: 10.14359/7815.
- [57] Wei, Y., Guo, W., Wu, Z., and Gao, X. Computed permeability for cement paste subject to freeze-thaw cycles at early ages. *Construction and Building Materials*, 244:118298, May 2020. ISSN 0950-0618. doi: 10.1016/j.conbuildmat.2020.118298.
- [58] Watanabe, K. and Mizoguchi, M. Amount of unfrozen water in frozen porous media saturated with solution. *Cold Regions Science and Technology*, 34(2):103–110, April 2002. ISSN 0165-232X. doi: 10.1016/S0165-232X(01)00063-5.
- [59] Yuan Jie, Lu Hang, Yang Quanbing, and Ling Jianming. Mechanisms on the salt–frost scaling of concrete. *Journal of Materials in Civil Engineering*, 29(3):D4015002, March 2017. doi: 10.1061/(ASCE)MT.1943-5533.0001448.
- [60] Sellevold, E. J. and Farstad, T. *Frost/Salt-Testing of Concrete: Effect of Test Parameters and Concrete Moisture History*. Nordic Concrete Federation, 1991.
- [61] MacInnis, C. and Whiting, J. D. The frost resistance of concrete subjected to a deicing agent. *Cement and Concrete Research*, 9(3):325–336, May 1979. ISSN 0008-8846. doi: 10.1016/0008-8846(79)90125-X.
- [62] Jebli, M., Jamin, F., Malachanne, E., Garcia-Diaz, E., and El Youssoufi, M. S. Experimental characterization of mechanical properties of the cement-aggregate interface in concrete. *Construction and Building Materials*, 161:16–25, February 2018. ISSN 0950-0618. doi:

707 10.1016/j.conbuildmat.2017.11.100.

708 [63] Callan, E. J. Thermal expansion of aggregates and concrete durability. *Journal Proceedings*, 48(2):485–504, February 1952. ISSN 0002-8061.
709 doi: 10.14359/11898.

710 [64] Cwirzen, A. and Penttala, V. Aggregate–cement paste transition zone properties affecting the salt–frost damage of high-performance concretes.
711 *Cement and Concrete Research*, 35(4):671–679, April 2005. ISSN 0008-8846. doi: 10.1016/j.cemconres.2004.06.009.

712 [65] Song, H., Yao, J., and Xiang, J. The role of aggregate and cement paste in the deterioration of the transitional interface zone of pervious
713 concrete during freeze-thaw cycles. *Case Studies in Construction Materials*, 16:e01086, June 2022. ISSN 2214-5095. doi: 10.1016/j.cscm.
714 2022.e01086.